EXPERIMENTAL REALIZATION OF KPZ DYNAMICS: SLOW COMBUSTION OF PAPER

BY
MARKKO MYLLYS

Academic Dissertation
for the Degree of
Doctor of Philosophy

To be presented, by permission of the
Faculty of Mathematics and Science
of the University of Jyväskylä,
for public examination in Auditorium FYS-1 of the
University of Jyväskylä on September 26, 2003
at 12 o'clock noon

Jyväskylä, Finland
September, 2003

Preface

Now after more than two decades of studying at several levels of education, it has come time to thank all the people I have had the honour to learn from, teachers, classmates and colleagues. Since 1992 I have studied in the Department of Physics, University of the Jyväskylä, and the last 8 years of that time I have been devoted to paper burning. From this nearly decade long interesting and fruitful project I would like to express my warmest gratitude first of all to Professor Jussi Timonen and also to other supervisors Docent Juha Merikoski and Dr. Olli-Pekka Kähkönen and to my long-time co-worker Dr. Jussi Maunuksela. This project would not have been so successful without very beneficial collaboration with especially Docent Mikko Alava and Professor Tapio Ala-Nissilä, but also with Professor Nikolas Provatas, Professor Marcel den Nijs, Dr. Meeson Ha, Professor Viktor Horvath, Dr. Rinke Wijngaarden and Mr. Marco Welling. I would also like to express my gratitude to the staff of the JYFL, especially to the skilled people in the mechanical workshop. For an inspiring and enjoyable working environment, I would like to thank all my work-mates in room FL348, especially Jani Maaranen.

From financial support I would like to thank the Graduate School of Material Physics, Academy of Finland and of course Professor Jussi Timonen, who has gathered up the resources for the whole project.

However most of all I want to thank my mother, brother, grand parents and Annukka, my beloved, from unending and unlimited support and encouragement.

Jyväskylä, September 2003

Markko Myllys

Abstract

Myllys, Markko
Experimental realization of KPZ dynamics: Slow combustion of paper
Jyväskylä: University of Jyväskylä, 2003, 114 p.
(Research report/Department of Physics, University of Jyväskylä,
ISSN 0075-465X; 5/2003)
ISBN 951-39-1575-1
diss.

There have been many recent advances in the theoretical understanding of kinetic roughening of interfaces. However, in very few experimental systems have these processes been studied in great detail and with good statistics. With our high resolution experimental set-up, described in this Thesis, we were able to gain a lot of information about slow-combustion fronts propagating in sheets of paper. The data gathered by us total to those of about a thousand individual burns, and involve experiments on four different paper grades. Temporal and spatial properties of the roughening interfaces were thoroughly studied by monitoring the interface width, correlation functions, structure factor, amplitudes of the correlation functions, and by determining the relevant parameters by an inverse method. Our results indicate that smouldering fronts in paper sheets asymptotically obey KPZ dynamics with roughening exponent $\chi \simeq 1/2$ and growth exponent $\beta \simeq 1/3$. A direct demonstration of the existence of the KPZ type of nonlinear term in the effective evolution equation for smouldering fronts was also provided by observing the effects of a columnar defect on the front shape. Below sample dependent crossover scales, higher 'apparent' temporal and spatial scaling exponents, and nontrivial effective noise, were observed. A natural source for this noise is the local mass fluctuations in paper sheets, and therefore also the correlations and distributions of these fluctuations were carefully investigated. Many but not all features of the short-range behaviour were qualitatively shown to be a consequence of these short-range correlations by direct numerical integration of the KPZ equation, where a real paper structure was used as the input noise.

Keywords slow combustion, scaling, noise, KPZ equation, non-equilibrium phenomena

Author's address   Markko Myllys
Department of Physics
University of Jyväskylä
Finland

Supervisors   Professor Jussi Timonen
Department of Physics
University of Jyväskylä
Finland

Docent Juha Merikoski
Department of Physics
University of Jyväskylä
Finland

Reviewers   Professor Knut Jørgen Måløy
Department of Physics
University of Oslo
Norge

Academy Professor Kimmo Kaski
Laboratory of Computational Engineering
Helsinki University of Technology
Finland

Opponent   Professor János Kertész
Institute of Physics
Budabest University of Technology and Economics
Hungary

List of Publications

A.I.   MAUNUKSELA, J., MYLLYS, M., KÄHKÖNEN, O.-P., TIMONEN, J., PROVATAS, N., ALAVA, M. J., AND ALA-NISSILA, T., *Kinetic Roughening in Slow Combustion of Paper*. Phys. Rev. Lett. **79** (1997) 1515–1518.

A.II.   MAUNUKSELA, J., MYLLYS, M., TIMONEN, J., KUITTU, M., ALA-NISSILA, T., ALAVA, M. J., AND PROVATAS, N., *Reply to the Comment of Amaral and Makse*. Phys. Rev. Lett. **80** (1998) 5707.

A.III.   MAUNUKSELA, J., MYLLYS, M., TIMONEN, J., ALAVA, M.J., AND ALA-NISSILA, T., *Kardar-Parisi-Zhang Scaling in Kinetic Roughening of Fire Fronts*. Physica A **266** (1999) 372–376.

A.IV.   MYLLYS, M., MAUNUKSELA, J., ALAVA, M.J., ALA-NISSILA, T., AND TIMONEN, J., *Scaling and Noise in Slow Combustion of Paper. Phys. Rev. Lett. 84 (2000) 1946–1949*.

A.V.   MYLLYS, M., MAUNUKSELA, J., ALAVA, M., ALA-NISSILA, A., MERIKOSKI, J., AND TIMONEN, J., *Kinetic Roughening in Slow Combustion of Paper*. Phys. Rev. E **64** (2001) 036101.

A.VI.   MYLLYS, M., MAUNUKSELA, J., MERIKOSKI, J., TIMONEN, J., AND AVIKAINEN, M., *KPZ equation with realistic short-range correlated noise*. Submitted to Eur. Phys. J. B.

A.VII.   MYLLYS, M., MAUNUKSELA, J., MERIKOSKI, J., TIMONEN, J., HA, M., AND DEN NIJS, M., *Effect of a columnar defect on the shape of slow-combustion fronts*. To appear in Phys. Rev. E.

The author of this Thesis has major contributions to the design, manufacture, testing and operation of the experimental set-up described in this Thesis. The author has developed measurement methods and collected all of the experimental data presented in this Thesis and in the enclosed articles in Appendices A.I–A.VII. The author performed the numerical simulations and data analysis reported in article A.VI, and participated in the writing of all the enclosed articles.

Contents

Chapter 1

Introduction

Better understanding of interface roughening has long excited the minds of physicists. Roughening of interfaces is often dominated by processes of stochastic nature and has many realizations both in the nature and in the laboratory, such as crystal growth, dielectric breakdown, fluid displacement in porous media, bacterial colony growth, fire front motion, vapour deposition, motion of magnetic flux lines in a superconductor etc. [17, 7]. Theoretical work has been focussed on stochastic differential equations that describe the essential features of the roughening processes. Because microscopical details have been removed by coarse graining, a single equation can describe a wide variety of phenomena. At the same time only relatively few reliable experiments have been done. The purpose of this Thesis is to review our experimental work [34,37,36,41,40] on slow-combustion fronts, the difficulties related to measurements in noisy systems, and to show that experimental evidence can indeed be found to support the idea of describing roughening processes by a stochastic differential equation. The work has been done in the Department of Physics at the University of Jyväskylä by Markko Myllys, Jussi Maunuksela, Juha Merikoski, Jussi Timonen and, at the initial phase of the work, also by Olli-Pekka Kähkönen, in collaboration with Mikko Alava and Tapio Ala-Nissilä from Helsinki University of Technology, and at the last phase of the work also with Meesoon Ha and Marcel den Nijs from the University of Washington.

Typically interfaces generated by a roughening process have fluctuations at many length scales and display within a certain, often rather short interval, a scale invariant structure, see *e.g.* the slow combustion fronts in Fig. 1.1. For a quantitative characterization of such structures Mandelbrot developed the concept of fractal geometry [32]. As a fundamental reason for why Nature produces scale invariant structures Bak, Tang and Wiesenfeld [4] proposed self-organized criticality (SOC). Roughening processes in Nature are typically far from equilibrium, and do not always comply with the assumptions behind SOC behaviour. There are however
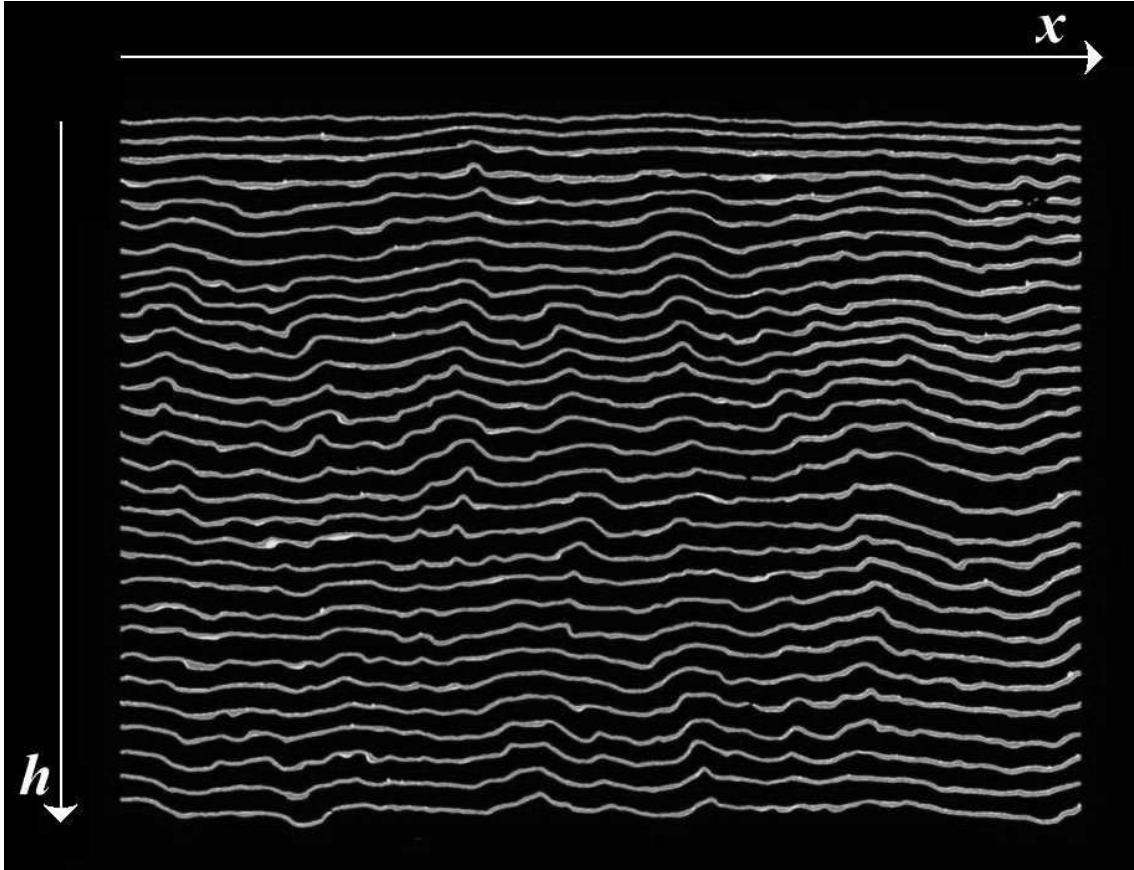
FIGURE 1.1 Digitised slow-combustion fronts with 10 s intervals.

well-established connections between SOC processes and rough interfaces [8, 51]. Noise can as such lead to scale invariant structures [26] which are often analysed by stochastic Langevin equations. Typically roughening processes can be classified into well-defined universality classes according to a few essential factors, *i.e.*, the nature of the local interface dynamics, and symmetries or conservation laws. Interfaces in each universality class display unique scaling properties which can be measured, for example, via interface width w,

$$w^2(L, t) \equiv \langle (h(x, t) - \bar{h}(t))^2 \rangle, \tag{1.1}$$

where $h = h(x, t)$ is a single-valued function, the position (or 'height') of the interface at point x and time t, $\bar{h}(t)$ is the average height at time t, and brackets denote ensemble averaging. In this Thesis we concentrate on one-dimensional interfaces propagating in a two-dimensional medium. The system size in the x direction is denoted by L.

If the interface evolves from an initially flat configuration, the scaling behaviour of its width can be described by the Family-Vicsek scaling relation [10],

$$w^2(t) \sim t^{2\beta} f(t/L^z) \sim \begin{cases} t^{2\beta} & \text{, for } \xi \ll L \\ L^{2\chi} & \text{, for } \xi \gg L \end{cases}. \tag{1.2}$$

Here, at early times, when the correlation length grows as $\xi \sim t^{1/z}$, the dynamics of the process are characterized by the growth exponent β. When the correlation length reaches the system size, the interface width w saturates. The roughness exponent χ describes the spatial scaling properties of the saturated interfaces. The values of the scaling exponents naturally depend also on the dimensionality of the interface.

Perhaps the most studied universality class is that of the nonlinear stochastic differential equation proposed by Kardar, Parisi and Zhang [22]. The famous KPZ equation is assumed to generically describe roughening processes with local propagation of the interface along the outward normal, and to be applicable in a wide variety of problems extending from propagating fire fronts to growth of bacterial colonies. Derivation of the KPZ equation from microscopic principles is tedious [17]. The terms included in this equation can, however, be justified by investigating the symmetry principles of the given roughening process, and by taking into account propagation along the local normal of the interface. To do this we first divide the continuum evolution equation into two parts,

$$\frac{\partial h(x,t)}{\partial t} = G[h(x,t)] + \eta(x, h(x,t), t). \tag{1.3}$$

Here $G[h(x,t)]$ is the deterministic part of the growth equation, which depends on the interface height, position and time. The relevant noise is denoted by the function $\eta(x, h(x,t), t)$. The first step in forming the deterministic part of the growth equation is to list the basic symmetries of the problem and to exclude terms that do not satisfy a necessary symmetry. The first symmetry, invariance under translation in time, rules out an explicit time dependence of G. The second symmetry, translation invariance along the growth direction, rules out an explicit height dependence of G. The third symmetry, translation invariance in the direction perpendicular to the growth direction, rules out an explicit x dependence of G. Rotation and inversion symmetries around the growth direction rule out odd-order derivatives in the coordinates. The up-down symmetry of h would rule out even powers of h, but this symmetry is often broken in non-equilibrium processes.

Terms that satisfy the relevant symmetry principles are thus the even derivatives $\nabla^{2n} h$, nonlinear terms like $(\nabla h)^{2n}$, and terms including both of them. Here n is

an integer. By including only the lowest order derivatives in the description of the asymptotic behaviour of the growth processes, we can write the KPZ equation in the form [7]

$$\frac{\partial h(x,t)}{\partial t} = \nu\nabla^2 h(x,t) + \frac{\lambda}{2}[\nabla h(x,t)]^2 + F + \eta(x, h(x,t), t). \tag{1.4}$$

The first term on the right hand side describes the 'bending stiffness' of the interface and ν is the related 'surface tension'. A diffusive relaxation of the interface would be described by a fourth-order derivative [53].

The second, nonlinear term does not satisfy the up-down symmetry, but its existence follows from propagation along the local normal of the interface. The actual form of this term follows from [7]

$$\delta h = [(v\delta t)^2 + (v\delta t\nabla h)^2]^{1/2} = v\delta t[1 + (\nabla h)^2]^{1/2}, \tag{1.5}$$

where $v\delta t$ is the infinitesimal propagation distance along the local normal of the interface, and its contribution in the vertical direction is ∇h. By assuming small slopes, $|\nabla h| << 1$, we can expand the local velocity from Eq. (1.5) as $v + v(\nabla h)^2/2$. The small-slope assumption is discussed in more detail later in Chapter 5 where the KPZ equation is solved numerically. The third term in Eq. (1.4) is the (vertical) driving force F. Due to the nonlinear nature of the growth equation $h(x,t)$ cannot as such be analytically solved in closed form, but many of its asymptotic scaling properties in $1 + 1$ dimensions can be obtained exactly [15, 24, 9, 44], and also by dynamic renormalization group methods [17], when η is uncorrelated white noise.

The form of the noise term $\eta(x, h(x,t), t)$ has a big influence on the scaling properties of the KPZ equation, and warrants therefore a more detailed discussion. We shall concentrate on the $(1 + 1)$-dimensional case. If the noise is Gaussian white noise and both spatially and temporally uncorrelated, (i.e.), $\eta = \eta(x,t)$ with $\langle\eta(x,t)\rangle = 0$ and $\langle\eta(x,t)\eta(x',t')\rangle = 2D\delta(x - x')\delta(t - t')$, the KPZ equation has [22] scaling exponents $\beta = 1/3$ and $\chi = 1/2$. In the saturated regime the spatial fluctuations of this 'normal' or annealed KPZ with Gaussian white noise are congruent to random walk, and the width of the interface depends on D, ν and L. If λ=0, Eq. (1.4) reduces to the linear Edwards-Wilkinson (EW) equation, which describes fluctuations of equilibrium interfaces. For this kind of noise the EW equation can be solved exactly, with the result $\chi = 1/2$ and $\beta = 1/4$.

Uncorrelated annealed noise may also be distributed by a power law instead of a Gaussian, $P(\eta) \sim \eta^{-(\mu+1)}$, where μ now characterizes the decay of noise amplitudes [17]. In this case rare events with large amplitude dominate the roughening as

the dynamics of the process is too slow to suppress these events. The nonlinearity of the KPZ equation amplifies the rare large events, and spreads their effects laterally. Below a critical value, $\mu < \mu_c$, the slower than Gaussian decay of noise amplitudes is relevant, and the roughness exponent χ is proportional to μ. Power-law distributed noise does not break the Galilean invariance, which leads to an additional scaling relation for the KPZ exponents, $\chi + \chi/\beta = 2$. Power-law distributed noise usually breaks the simple self-affine morphology of the interfaces, and their 'multi-affine' properties are reflected in an infinite series of exponents instead of one [7].

Yet another possibility is long-range correlated annealed noise [17]. If noise is only spatially correlated, $\langle \eta(x,t)\eta(x',t') \rangle \sim |x - x'|^{2\rho - 1}\delta(t - t')$, Galilean invariance holds, and $\chi = (1 + 2\rho)/3$ for $1/4 < \rho < 1$. For smaller values, $\rho < 1/4$, the normal KPZ scaling is recovered. Temporal correlations break the Galilean invariance and induce additional complications, but relations for both scaling exponents can still be found [38].

In the case of spatially quenched noise, $\eta = \eta(x, h(x,t))$, the KPZ equation displays a depinning transition at a critical value of the driving force F_c [3, 38]. Depinning of the interface can be considered as a critical phenomenon, where the average velocity vanishes with a power law $v \sim (F - F_c)^\theta$. For $F < F_c$ the interface is pinned to one of the many locally stable configurations. At $F = F_c$ the scaling properties of the pinned interface depend on the behaviour of the nonlinear term meaning that two new universality classes are formed. In the QKPZ universality class the coefficient λ diverges at the pinning transition and interface roughening can be mapped onto the directed percolation depinning (DPD) problem, by which the scaling properties of the interface are determined by the spanning directed percolation cluster [31, 43]. The scaling exponents for the pinned interfaces are $\chi = \beta \approx 0.63$. If the nonlinearity vanishes at $F = F_c$, $\lambda = 0$, roughening is described by the linear 'quenched' EW equation (QEW) with exponents $\chi \approx 1$ and $\beta \approx 0.88$ for both the pinned and the moving interfaces just above F_c [3]. Quenched noise together with nonlinearity leads naturally to power-law distributed noise, and therefore interfaces then typically have 'multi-affine' scaling properties [7]. This means that in the QKPZ case moving interfaces just above F_c are not self-affine, but the second moments of the height-height correlation functions (Eqs.4.3 and 4.2) scale with exponents $\chi \approx \beta \approx 0.75$ [30]. With a strong enough driving force, $F > F_c$, the interface no longer gets pinned by the local disorder, and the normal KPZ case is recovered asymptotically [30].

In several experimental studies, *c.f.* Chapter 2, no clear asymptotic KPZ scaling was however found. Also, there were many open questions related to the obtained anomalous scaling exponents, from both experiments and numerical studies.

Therefore, in 1995 we started to construct an experimental set-up to study the expected KPZ-type behaviour of slow-combustion fronts in sheets of paper [46]. The task turned out to be quite challenging and demanding. After careful design and construction of the experimental set-up, which took the best part of a year, we could do our first experiment, and since then we have burned hundreds of samples and gained quite a lot of insight in the kinetic roughening of interfaces, as will be seen from the rest of this Thesis.

The outline of the Thesis is the following. Above we have briefly described the theoretical motivation for our work. Chapter 2 includes a short description of other experimental work on roughening interfaces. Chapter 3 is a detailed description of our experimental set-up and the measuring procedure. Our main results are presented in Chapter 4, and numerical simulations of the KPZ equation with real noise in Chapter 5. Chapter 6 comprises a brief conclusion and a discussion of possible future work.

Chapter 2

Results from other experiments

Various experiments on kinetic roughening in systems such as surface growth, erosion, imbibition (paper wetting), and fluid invasion have mostly failed to demonstrate the 'normal' KPZ scaling. To better appreciate this fact, some of these experiments are briefly discussed in this Chapter.

J. Zhang *et al.* performed in 1992 the first reported experiment on the kinetic roughening of slow-combustion fronts in paper. They used a thin (9.1 g/m^2) lens paper manufactured by Whatman. Paper samples of size (460×1100) mm^2 where treated with potassium nitrate (KNO$_3$) to facilitate the propagation of slow-combustion fronts. They found the appropriate range for the KNO$_3$ concentration to be (0.87-1.6) g/m^2, yielding mean front velocities between 5.5 and 8.2 mm/s. Results were reported for a KNO$_3$ concentration of 0.95 g/m^2. Paper samples were placed vertically between metallic holders and ignited from the bottom. Experiments where done under normal room conditions without any forced ventilation. A photograph of a front was taken for 15 individual burns at a fixed time after the ignition. These photographs were then digitised with the number of pixels 3000×512. The front was defined as the boundary between the burning and intact areas of the sample. The scaling properties of the fronts were analysed from the behaviour of the front width $w(L,t)$ as a function of front length L. They found good scaling of the surface width, $w \sim L^{\chi}$, over nearly two decades, with an anomalous value for the roughness exponent χ=0.71(5) [56].

Another recent (2001) paper burning experiment, by Balankin and Matamoros, also displayed anomalous scaling of fire fronts (roughness exponent $\chi \sim 0.83$). They burned with flames 400 mm long samples of Secant paper (200 g/m^2) with sample widths of 12 to 80 mm. After the propagating flame front line ($\bar{v}$=3.0(1) mm/s) reached the middle of the sample, it was quenched, and the resulting 'post-mortem' front was scanned for later analysis. The front position was determined from both the leading and the trailing edge of the burned area. The spatial scaling properties

of the fronts such determined were analysed using the sample averaged interface position, a variogram and power spectrum methods [5].

Several experiments have been done on displacement of a fluid by another in a porous medium. The interface between the two fluids also displays scaling behaviour for certain ranges of properties of the fluids and the porous medium. Rubio *et al.* [49] made experiments on the water-air interface driven through effectively two-dimensional systems of tightly packed glass beads in 1989. They found the value β=0.73(3) for the growth exponent from the time-dependent interface width $w(L,t)$. Horvath *et al.* [19] made a similar kind of experiment in the following year. They used glyserol instead of water, and the system size was (24×100) cm^2, to be compared with the size (15×55) cm^2 used in Rubio's experiments. Horvath *et al.* determined both roughness and growth exponents by studying the height-height correlations. For the growth exponent they found $\beta \simeq 0.65$, which again is higher than the KPZ value. For the roughness exponent χ they found two regimes, with $\chi_{SR} \simeq 0.81$ at short range and $\chi \simeq 0.49$ at long range. In both these experiments fluid was injected through a system of glass beads. A different situation can be arranged by using capillary forces instead of a constant pressure as the driving force. These imbibition experiments were also found to produce anomalously high values for the scaling exponents, and their results were explained by the DPD model [2,20].

Another observation of two scaling regimes with a crossover to asymptotic KPZ scaling was that by R. Surdeanu *et. al.* [50] in 1999. They studied kinetic roughening of magnetic flux fronts penetrating a high-T_c thin-film superconductor. A magnetic field was applied between the short sides of a $YBa_2Cu_3O_{7-x}$ film on $NdGaO_3$ substrate of size (1.5×8) mm^2. High resolution magneto-optic techniques were used to obtain a two-dimensional image of the local magnetic field at the surface of the sample. Pictures of the local magnetic field were recorded at 1mT intervals, and the front line was determined as the borderline between the region where vortices are present and the flux-free region. The scaling properties of the fronts were analysed using both the interface width $w(L,t)$ and the two-point correlation function. Both the roughness exponent χ and the growth exponent β displayed crossover from anomalous scaling to KPZ scaling. The measured short-range scaling exponents were β_{SR}=0.65 below a field strength of ~ 10 mT (time can be measured in terms of the continuously varying field strength), and χ_{SR}=0.64, below a crossover length scale of 0.06 mm. The long-range scaling behaviour was found to be of KPZ type with χ=0.46 [50].

In order to gain the true scaling properties of the roughening interfaces, a proper averaging over noise should be done. For example, we found it necessary to average over at least ten different samples with a few thousand front images for

each sample to obtain reliable scaling behaviour for slow-combustion fronts in paper. J. Zhang *et al.* took one photograph of each burn at a fixed time after the ignition, and the results were averaged over 15 individual burns. Balankin and Matamoros scanned the 'post-mortum' fire front for at least 50 experiments. Rubio *et al.* obtained 30 images from each fluid-displacement experiment, and they used 10 different capillary numbers (Ca) and three different bead sizes. Horvath *et al.* [19] used a CCD-video camera with a sampling rate of 0.28 s to produce several thousand fronts for one fluid-displacement experiment with fixed Ca and bead size. Surdeanu *et. al.* [50] used two different samples and they recorded over one hundred fronts for both samples. Based on our experience, the averaging performed in Refs. [19, 50] approaches an appropriate level, while in all the other quoted experiments limited averaging may have affected the results. On the other hand, we found it necessary to extend the averaging even much beyond the level of Refs. [19, 50].

All the experiments described above have produced short-range scaling exponents significantly higher than those for the KPZ equation, with or without crossover to KPZ values at long range. Various explanations have been suggested as for why the KPZ scaling has generally not been found, and most of them are concerned with the characteristics of the noise. In addition, when studying the universality classes describing only the most essential factors of the process, the asymptotic scaling regime should be reached, and it depends on both the dynamics and the noise characteristics. Therefore, experiments should involve long enough time and length scales and proper (extensive) averaging over noise to obtain reliable estimates, *e.g.*, for the scaling exponents χ, β and z. There are also other quantities and distribution functions that can be used to probe the scaling properties. These properties will as well be considered in this Thesis.

Chapter 3

Measuring procedures

The goal of our measurements was to analyse in detail the scaling properties of propagating interfaces at long enough time and length scales, and to produce enough of data for extensive averaging over noise. To this end we considered slow-combustion (smouldering) fronts moving in sheets of paper which was shown to asymptotically obey the KPZ dynamics [47]. Paper is a common inhomogeneous material and the propagation speed of slow-combustion fronts in them can be made conveniently slow (v=0.5-10 mm/s; see Fig. 1.1). This Chapter is divided into three sections according to how the measuring process proceeds in practice. The first section deals with the properties of the paper samples and how the samples were prepared to exhibit slow flameless burning. The experimental set-up and some essential mechanical details are introduced in the second section, while the recording of the fronts is discussed in the third section.

3.1   Properties of the samples

At the early stage of this work, propagation of smouldering fronts was tested in many paper grades including cigarette paper, filtering paper, light weight coated paper (LWC), other coated paper grades and copier papers of basis weights 70 g/m^2 to 200 g/m^2. For more detailed studies [34,36,41,40], four paper grades were chosen based on a suitable span of properties to check the universality of the results and on easy availability. The first samples burned by smouldering were made of cigarette paper of basic weight 28 g/m^2, manufactured by UPM-Kymmene (Tervakoski Paper Mill). Another two of them were ordinary copier papers of basic weights 70 g/m^2 and 80 g/m^2, manufactured by UPM-Kymmene (Tervakoski Paper Mill) and Metsä-Serla (now M-real, Kangas Paper Mill), respectively. The fourth paper grade was thin lens paper of a basis weight of only 9.1 g/m^2, manufactured by Whatman
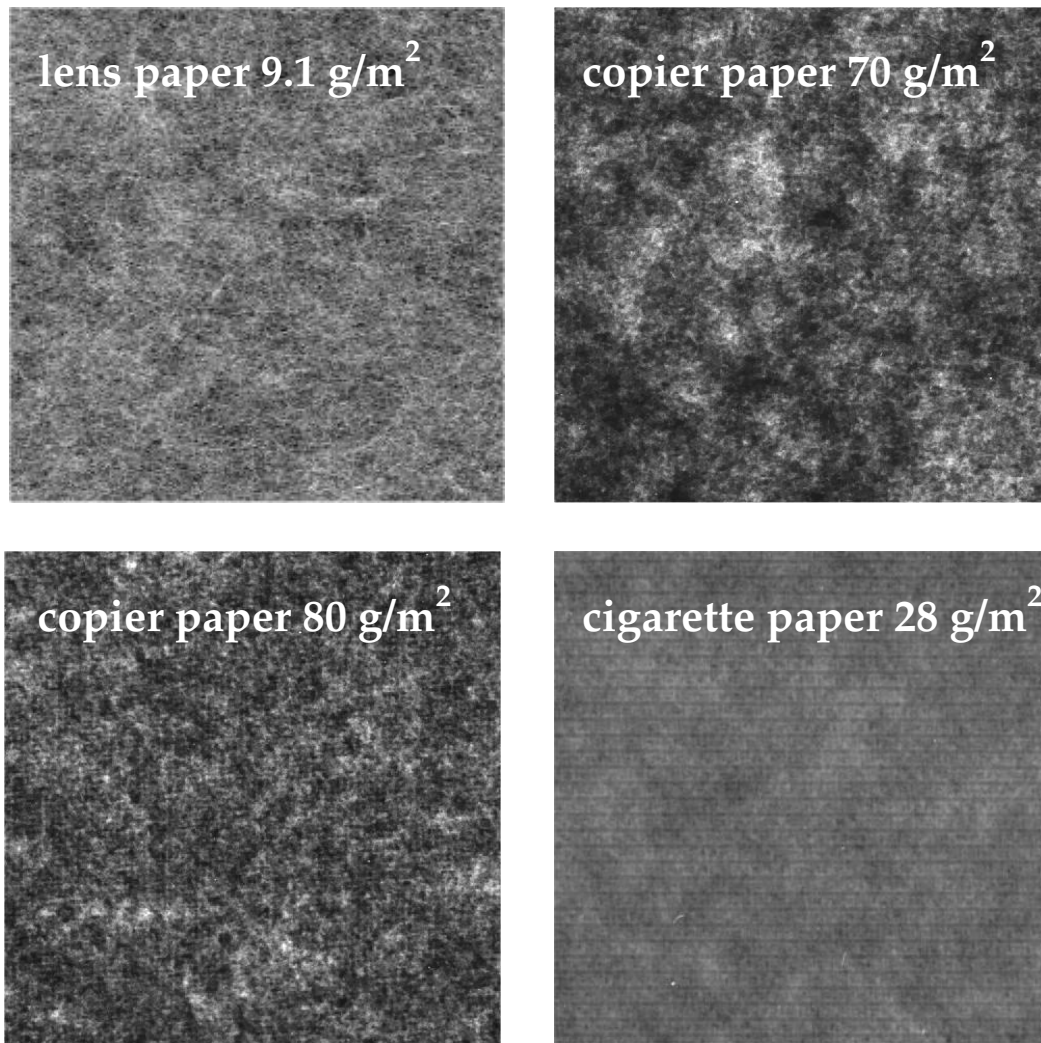
FIGURE 3.1 β-radiographs of paper samples of size (30×30) mm^2. The image of the lens paper is made by optical scanning.

Paper Ltd. An essential property of the samples was the variation in the local mass, which naturally affects the local velocity of the front and is therefore one source for the noise discussed in Chapter 1 above. The local mass distributions and their correlations were analysed from β-radiographs like the ones shown in Fig. 3.1. The measurement is based on the transmission of β radiation, whose attenuation coefficient is inversely proportional to the local mass, but is not sensitive to the composition of the samples, e.g. fibres and mineral fillers. β-radiographs for the copier papers were taken from paper samples of size (177×455) mm^2 using a spatial resolution of 0.085 mm, and for the cigarette paper the sample size was (385×500) mm^2. For the lens paper we used optically scanned images of size (210×540) mm^2, which provide an approximative description of the local mass variations.
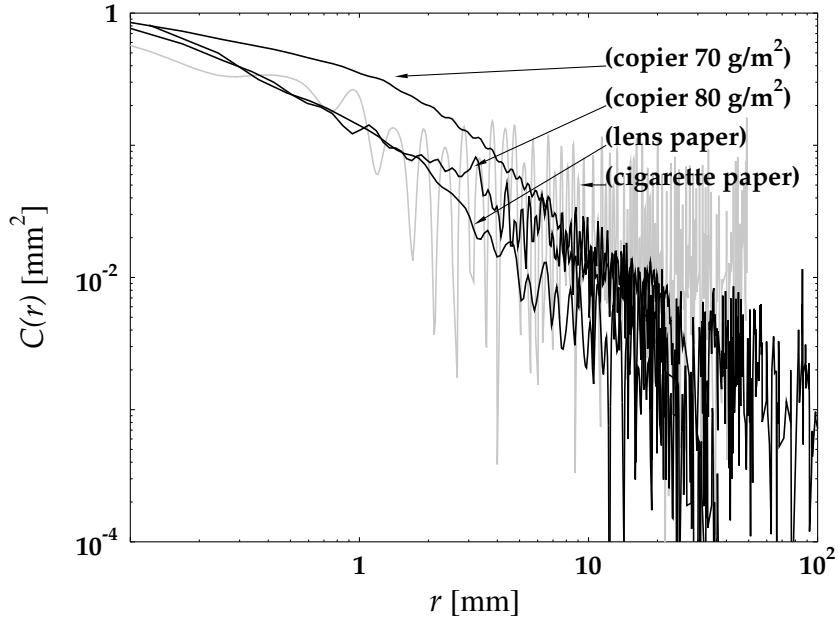
FIGURE 3.2 Spatial correlation functions for the paper samples shown in Fig. 3.1

Correlations were analysed by using the two-point mass fluctuation correlation function defined by

$$C_m(\vec{r}) = \langle [m(\vec{x}) - \overline{m}][m(\vec{x} + \vec{r}) - \overline{m}] \rangle, \tag{3.1}$$

where $m(\vec{x})$ is the local mass, $\overline{m}$ its overall average, and brackets denote spatial averaging. Correlation functions C_m for four paper grades with the best statistics available are shown in Fig 3.2. Evident short range correlations for thin grades of paper arise from the highly asymmetric shape of the cellulose fibres and from the flocculated structure of the fibre network, and typically extend to somewhat beyond the fibre length, *i.e.*, to a few millimetres [48]. The periodic structure of the cigarette paper (Fig. 3.1) is also seen in the correlation function of Fig. 3.2, and because of this unwanted property we did not use cigarette paper in later studies. Some results on cigarette paper are given in Ref. [34]. Another essential feature of the samples was the ability to sustain the propagation of smouldering fronts. In cigarette paper a secret recipe of chemicals was already added in the manufacturing process to avoid flames when ignited. For the same purpose we used potassium nitrate (KNO_3) as in Ref. [56] earlier. Potassium nitrate, normally used as a component in fertilizers and explosives, releases oxygen when its temperature exceeds about 400 °C, which enables slow flameless combustion in paper when added by a sufficient amount. For thick paper grades made of pure cellulose, such as filter papers, even addition of KNO_3 was not enough to initiate slow combustion. Calcium carbonate ($CaCO_3$) and

other mineral fillers with high heat capacity and conductivity, used *e.g.* in copier papers, improve slow combustion by reducing the dissipation of heat from the burning paper through improved heat storage and conduction.

The KNO_3 treatment was done by using several techniques. Copier paper samples (450×530) mm^2 were embedded in an aqueous solution of KNO_3 for 5 minutes. The amount of the solution taken in by the samples, in a typical concentration of about 5 g/l, was measured to estimate the final amount of KNO_3 in the samples. After embedding, the samples were placed on a table until most of the water was evaporated, after which they were dried under a heated press to maintain their planar shape. After a day the relative moisture contents of the samples was saturated to the level of humidity in laboratory air, and samples of specified size were cut out of these larger sheets to avoid a higher absorbed amount of KNO_3 at the boundaries. The appropriate amount of KNO_3 in copier papers was approximately 0.8 g/m^2. Due to the lower basis weight and much more porous structure, drying of the KNO_3 solution from lens paper was not homogeneous over the sample, leading to an inhomogeneous concentration distribution of KNO_3. Food dye, patent blue, was used as an indicator to find ways to add KNO_3 uniformly to the lens paper samples. The most uniform KNO_3 distribution was achieved by spraying both sides of the samples on a hot metal plate with a KNO_3 solution of concentration 20 g/l. The metal plate was heated up to 100 °C so that the fine spray of the KNO_3 solution was immediately dried from the sample. The amount of the added KNO_3 was measured by weighing four plastic plates (placed on each side of the paper sample during spraying) before and after spraying, with an accurate analytical balance. For lens paper, the amount of KNO_3 sufficient for slow combustion was (0.2-0.9) g/m^2, leading to front velocities (6.5-10.5) mm/s. In Fig (4.8) the average velocity of the lens paper fronts is shown as a function of the KNO_3 concentration.

The distributions of fillers ($CaCO_3$) and added KNO_3 were measured with the laser ablation method [16] on several thin layers of both lens and copier paper samples. Within the spatial resolution of the method (0.2 mm), we found no correlations in the variations of the KNO_3 or $CaCO_3$ concentrations in any layers. The mean level of the emitted potassium intensity in the laser ablation measurements was found to be greater in lighter papers, and therefore stronger aqueous solutions of KNO_3 were used for heavier paper grades. In addition, β-radiographs were taken from copier-paper samples after and before a 5 min soaking in a KNO_3 solution to ensure that the mass distribution did not change detectably in this process.

To summarize, we found no spatial correlations in the filler concentration, the local variations in the mass, or the potassium nitrate distributions, beyond a few millimetres, except for the cigarette paper.

3.2   Combustion chamber

The experimental set-up, shown as a schematic diagram in Fig. 3.3, consists of a combustion chamber, a sample holder and a camera system with a necessary computer hardware and software. The framework of the combustion chamber, of size $(1000 \times 1000 \times 500)$ mm^3, is made of aluminium L-profile. One side of the chamber is covered by a detachable aluminium plate for installing the paper samples, and the opposite side is made of glass to visually observe the experiments. Other sides are covered by aluminium plates with movable inlets and outlets for air. Ventilator ducts are formed between the outer covering and a combination of an aluminium screen plate and a filtering matt, which make the incoming air flow more laminar. Combustion gases are removed by a controllable fan and filtered electrostatically. In
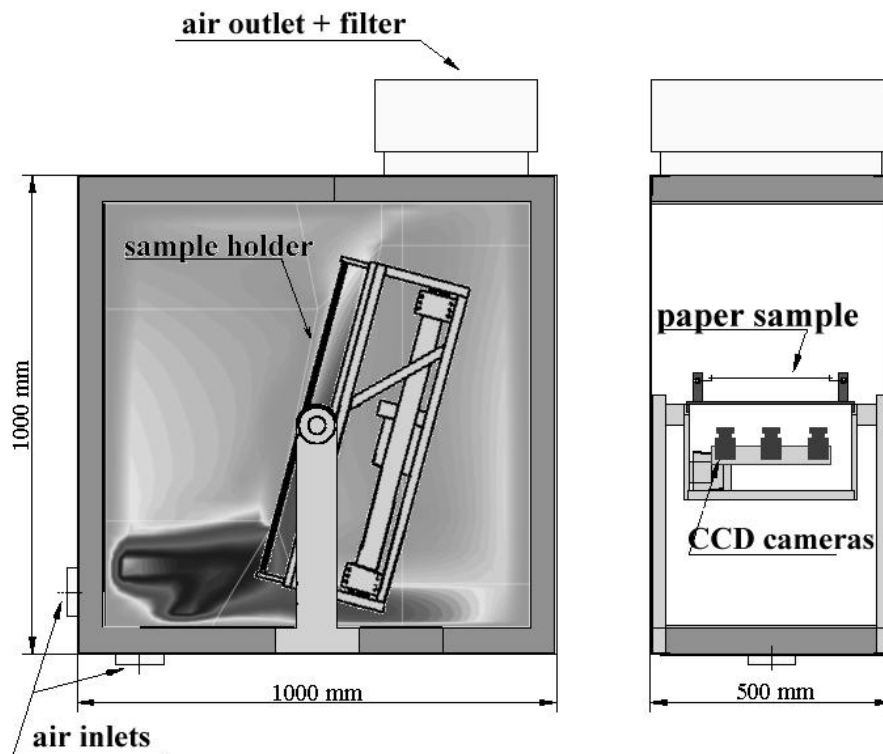

FIGURE 3.3 A schematic diagram of the experimental set-up.

the middle of the chamber there is a detachable paper holder, designed for a maximum paper size of (400×600) mm^2 (Fig. 3.4). The sample holder is an open metallic frame, where the paper samples are attached from both sides to keep them planar during combustion (Fig. 3.4). The copier paper samples were attached to the paper holder with thin needles to minimize the heat loss from the burning front. Needles are forced through the edges of the paper samples to ensure steady fixing. Extra heat loss from the boundaries was first compensated with heat filaments that fol-
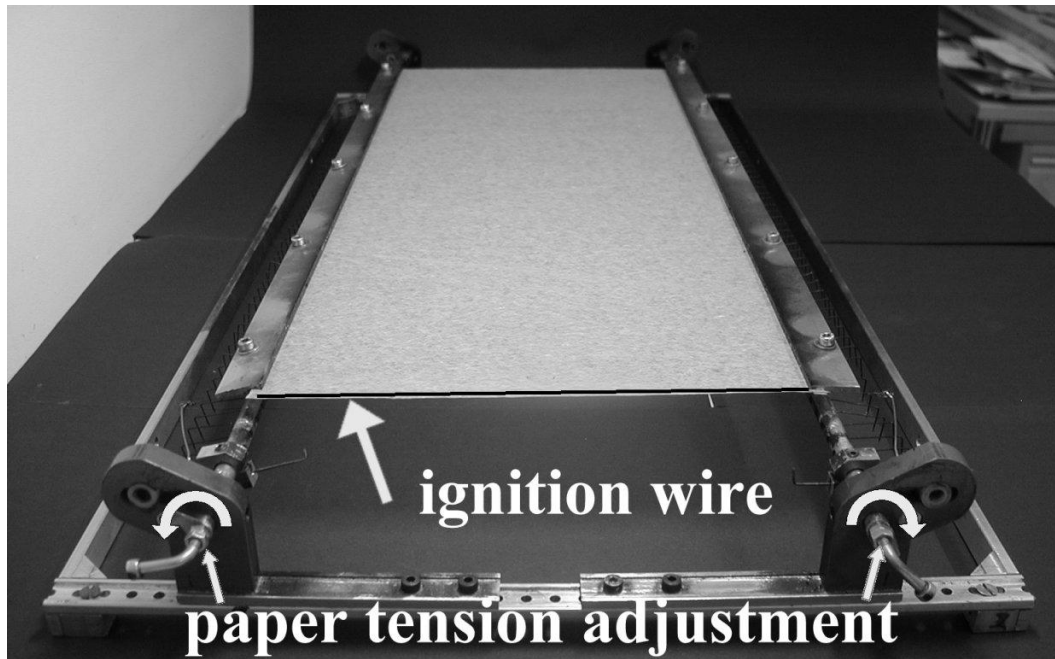
FIGURE 3.4 The detachable paper holder with a lens paper sample.

lowed the combustion front. The filament shown in Fig. 3.5 was moved by rotating
a threaded bar by a DC motor. A typical heating power for one filament was about 10
watts. Later the edges of the samples were folded (see Fig. 3.5) to achieve a better
heat loss compensation. Copier paper samples had to be placed the right face to-
wards the cameras, because ashes predominantly bend only to one side of the sheet.
Thin lens papers were attached to the same holder but between two aluminium
bars. This arrangement was not an ideal way to deal with boundary conditions, but
our aim was to repeat the experiments reported in [56] and furthermore, lens paper
was not so sensitive to the boundary conditions. In both cases paper tension was
controlled by turning the bar shown in Fig. 3.4. Ignition of the samples was done
by heating a tungsten wire (Fig. 3.4) with a DC power supply. To attain a straight
smouldering front, the ignition temperature must be carefully adjusted. Too high a
temperature caused the sample to burst into flames, and with too low a temperature
the sample was ignited unevenly. The proper temperature range, red-hot (600-700)
°C, for the tungsten wire of diameter 0.38 mm and length 400 mm, was achieved
with a power of 80 W. The tungsten wire was attached at both ends to springs to
keep it straight despite of its expansion while heated. The paper holder can be ro-
tated with respect to the adjustable air flow so that convective transfer of heat ahead
of the propagating front can be regulated, and other flow-dependent features of the
process can be optimized. Air flows in the chamber were simulated with a compu-
tational fluid dynamics software CFX 4, to ensure the conditions remained similar
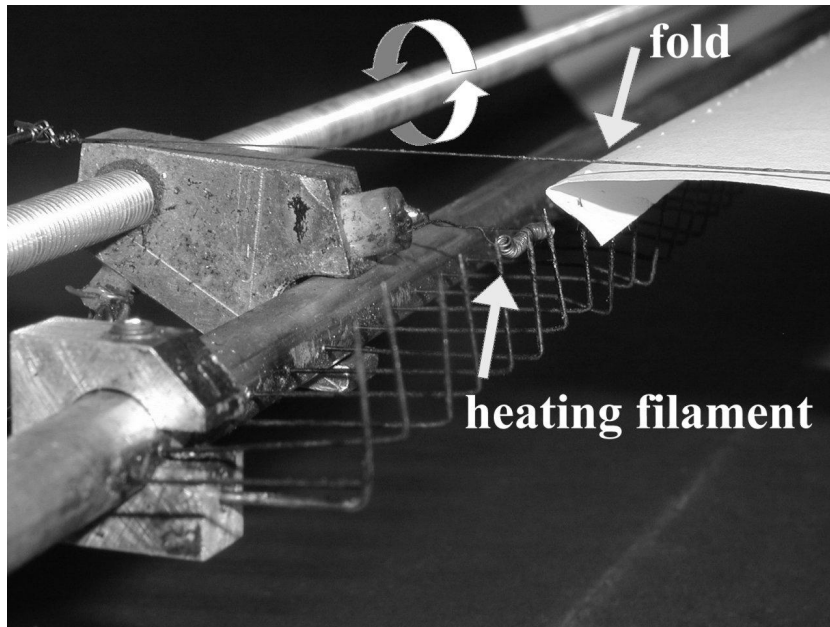
FIGURE 3.5 A close view of the fastening of copier paper. Both methods for compensating the heat losses at the boundaries are also shown: the heating filament and the folds at the sides of the sample.

for the whole sample, although simple visual observation of the combustion gases gave even more accurate information about the flow conditions in the chamber. Simulated flow velocities in the chamber are shown in the Fig. 3.3. The typical flow rate for the copier paper samples was (10-15) l/s, while lens paper samples were burnt without forced ventilation.

3.3   Recording of the fronts

The data recording system was developed during the work along with advancements in both the computer system and the charge-coupled device (CCD) cameras. In the initial set-up the procedure started by recording the fronts with a CCD camera and an SVHS video recorder. Afterwards, accurate front positions were determined from the recorded images for detailed analyses.

The present camera system is based on three black and white CCD cameras (Pulnix TM-6EX), which are moved with regular intervals along with the moving front. Cameras with overlapping image fields were attached to a stand that was operated with a pneumatic cylinder (Fig. 3.6). The control of the camera movements, boundary heating filaments and forced ventilation was carried out with a multifunction I/0-board (National Instruments: AT-MIO-16DE-10) installed on the attached computer. The control programs were written with the LabVIEW measurement and
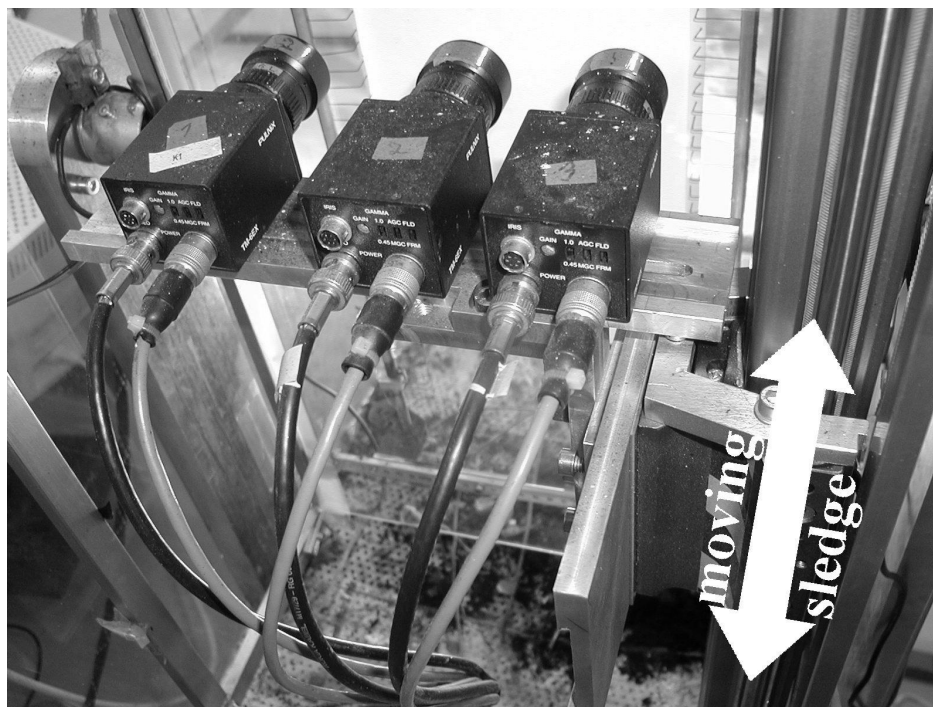
FIGURE 3.6 The moveable camera system.

automation software. Three parallel cameras, with a resolution of (758×581) pixels, were synchronized to take simultaneous images with a maximum frequency of ten images per second. The images were transferred to the attached computer with a frame grabber board (IC-COMP) manufactured by Coreco Imaging. Because experiments where done in darkness, the only visible objects in the images were the combustion fronts. By omitting the dark background we were able to compress the size of each individual frame file from 431 kB to approximately 15 kB. Compression was done on line and the compressed images were stored on the hard disk. After the experiment the front line was determined from each frame by first finding the pixels brighter than a given gray-scale value. A single-valued front line was then fitted into the brightness profile. For the intervals, in which a front line could not be identified, a straight line was fitted by interpolation (see Fig. 3.7). Cylindrical image distortions caused by the lenses were corrected by using nonlinear warping. The method requires a collection of 2D landmark points, whose true locations are known together with their distorted images. These were then used to define a global warping function. Using this warping function, corrections were made into the position data of the individual cameras before joining the images. Typical defects in the recorded images are shown in Fig. 3.7. Sparks and other rare defects were moved out afterwards from the data files by using a robust filtering method based on minimising a cost function of the local and temporal gradients [33].
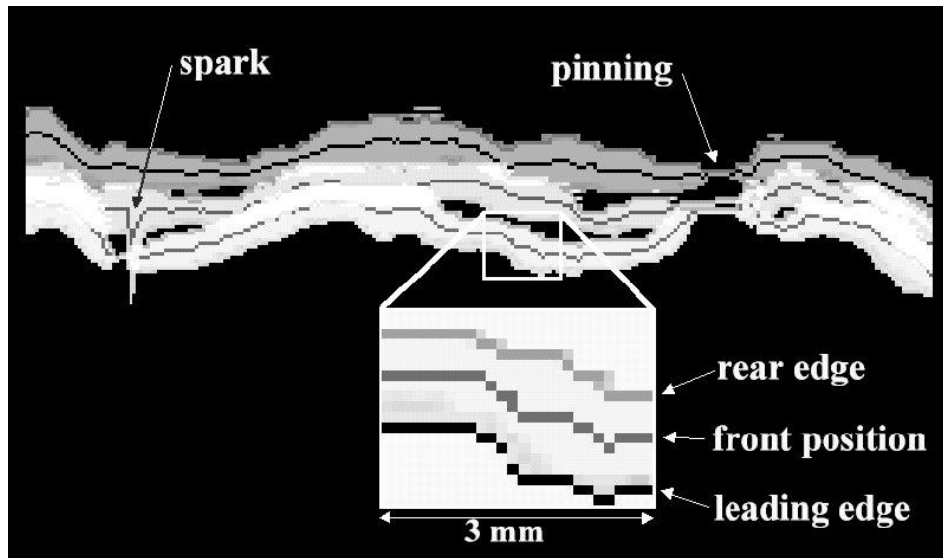
FIGURE 3.7 A sequence of three digitised fronts with a time step of 0.2 s. Occasional defects in the front detection, a spark and a pinning site, are clearly visible.

Because of many potential sources for failure in the experiments, the total amount of acquired burns was around one thousand. The first problem was an accurate control of the KNO_3 concentration: too high an amount caused the sample to burst into flames, and too small an amount caused fronts to quench or pin. In addition, recording and detecting of the actual front positions failed occasionally because of uneven paper tightness (wrinkles in samples), ash formation which obscured the fronts from the cameras, wrong camera placements, or too rough an interface which caused some parts of the front to be out of camera view. Also, an even ignition turned out to be quite a challenging task. Successful experiments required accurate sample preparation, careful mounting of the paper sample, even ignition, correctly calibrated camera system (movements, 2D landmarks for distortion correction), and a lot of time spent in the dark laboratory.

Chapter 4

Experimental results

A great amount of data gathered over several years have been studied from many perspectives. The surface width $w(L, t)$, correlation functions $C(r, t)$, and the structure factor $S(k)$ were used to estimate the scaling exponents χ and β. The amplitudes of the correlation functions and an inverse method, *e.g.*, were also used to determine the parameters of the KPZ equation. Distributions and correlations of the surface height and velocity fluctuations were used to analyse the effective noise. First return probabilities of surface fluctuations provided an independent way to characterize the scaling properties [35]. A more detailed description of how these quantities were determined can be found in the Thesis of Jussi Maunuksela [33]. Therefore, only the main results are presented in the present Thesis. Most of the results are reported in the included publications except for the results in the last section on the pinning transition and avalanches. These phenomena need a more detailed analysis, but a preliminary account of them is given here for a more comprehensive view of the properties of smouldering fronts.

Our results for three different paper grades are presented in this Chapter. The first two grades are copier papers with basic weights of 70 g/m^2 and 80 g/m^2, and with a KNO$_3$ concentration of approximately 0.8 g/m^2. The samples of both copier paper grades were placed at a 20° angle from the vertical direction and ignited at the top of the sample. A slight air flow (~ 10 l/s) was applied opposite to the propagation direction of the fronts to minimize convective heat transfer ahead of the front. Both boundary heating methods described in Chapter 3, the heating filaments and folding of the edges were used. The size of the copier paper samples was (390×500) mm^2. The width of the recorded area was 310 mm and the width of the area used in the analyses of this Chapter was 270 mm with a pixel resolution of 0.135 mm. The time step in front recording was 4.2 seconds for the 70 g/m^2 samples, and 0.2–1.25 seconds for the 80 g/m^2 samples, and the results were averaged over 10 and 8 different samples, respectively. Averages were thus taken over 2000 fronts for the 70

g/m^2 paper and over 40000 fronts for the 80 g/m^2 paper.

The measurement set-up for the lens paper (9.1 g/m^2) was similar to that used if Ref. [56]. There was no forced ventilation and the samples were ignited from the bottom. A typical KNO$_3$ concentration was around 0.8 g/m^2 and it was applied by spraying. For samples with size (400 × 550) mm^2, the saturated region (see Eq. (1.2)) was not reached, and therefore the sample size was reduced in this case to (225× 550) mm^2. Ten fronts were recorded during every second with a pixel size of 0.138 mm, and the results were averaged over 32 different samples. Averages were thus taken over 20000 fronts. Lens paper was not very sensitive to the boundary conditions so that there was no need for boundary heating, and the whole widths of the samples were used in the analyses below.

4.1   Scaling properties

A straightforward way to estimate the growth exponent β is to use the scaling properties of the front width $w(L, t)$ as defined in Eq. (1.2). In Fig. 4.1 the front width $w(t)$ is shown in a log-log plot as a function of time for the three paper grades. Uneven ignition disturbs the early time dynamics of the roughening process and therefore the KPZ type scaling of the front width is seen only after a short interval after ignition. Front widths w for individual lens paper samples indicate large fluctuations between different burns. For copier paper samples fluctuations are smaller leading also to the lower saturation width despite the fact that the system size L was almost double for the copier papers. The symbols used in the figures for different paper grades are the same throughout this Chapter, ★ = lens paper (9.1 g/m^2), ○ = copier paper (70 g/m^2) and □ = copier paper (80 g/m^2). Also the roughness exponent χ can be determined from the front width w. The results for χ are given in the enclosed publication [40]. In measurements where only one system size L is used, like in our set-up, the front width is determined for and averaged over subsystems of sizes ℓ so that $w^2(\ell, t) = \langle\langle[h(x, t) - \langle h(x, t)\rangle_\ell]^2\rangle_\ell\rangle$.

In addition to front width, especially when there are large fluctuations in the data as in the case of lens paper (see Fig. 4.1), useful information can also be gained from the qth order two-point height-difference correlation functions

$$C_q(r, t) = \langle\overline{[\delta h(x', t') - \delta h(x' + r, t' + t)]^q}\rangle_{x',t'}, \tag{4.1}$$

where q is a positive integer, $h(x, t)$ is the height of the front at point x and time t, $\delta h(x, t) \equiv h(x, t) - \overline{h}(t)$, the bar denotes an average over a front and the brackets an average over all configurations (fronts and burns). For this quantity, one can define
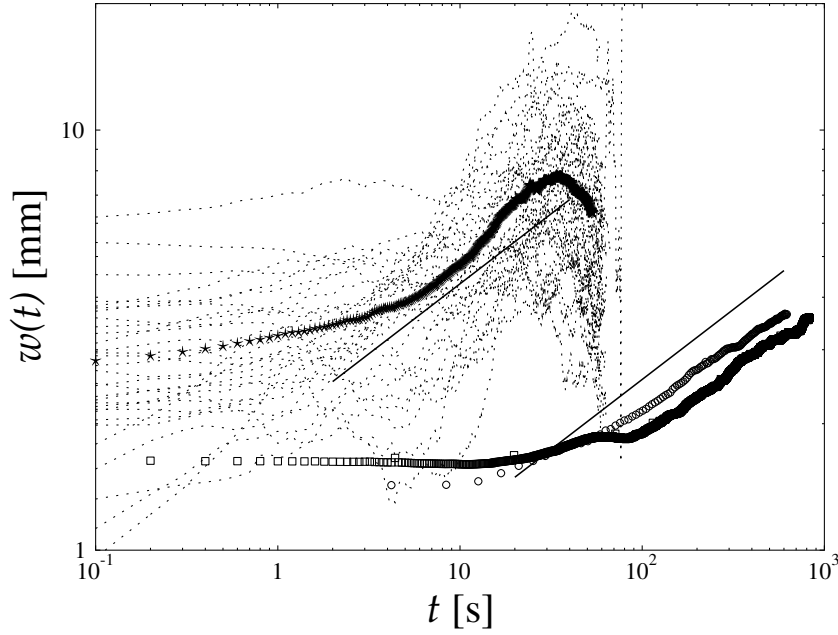
FIGURE 4.1 Time evolution of the front width for three paper grades. The slope of both solid lines is the KPZ value for the growth exponent, $\beta = 1/3$. The symbols used in the figures of this Chapter are: ★ = lens paper (9.1 g/m^2), ○ = copier paper (70 g/m^2) and □ = copier paper (80 g/m^2). Individual lens paper burns are denoted by dotted lines and the average of them by stars.

two scaling limits,

$$G_q(r) \equiv C_q(r,0) \sim Ar^{\chi_q}, \tag{4.2}$$

and

$$C_q(t) \equiv C_q(0,t) \sim Bt^{\beta_q}, \tag{4.3}$$

which can be used to estimate the roughness and growth exponents, respectively. In the saturated regime the functions $G_q(r)$ can be averaged over all times (steady-state configurations), and $C_q(t)$ over all spatial points. The saturation time t_{sat} was estimated from the averaged surface width $w(t)$. For copier papers the saturated regime was approximately the last two thirds and for the lens paper the last half of the data. For simply self-affine fronts $\chi_q = q\chi$ and $\beta_q = q\beta$, with χ and β the desired scaling exponents. The second moment of the spatial correlation function $G_2(r)$ is shown in Fig. 4.2(a), and the temporal correlation function $C_2(t)$ in Fig. 4.3(a). In both correlation functions (Figs. 4.2 and 4.3) two separate regimes of possible scaling were found. The asymptotic behaviours of the correlation functions show clear KPZ-type scaling for all paper grades, while at short time and length scales anomalously large exponents were found. Accurate determination of the scaling exponents was complicated by the "intrinsic" width of the fronts caused mainly by structural
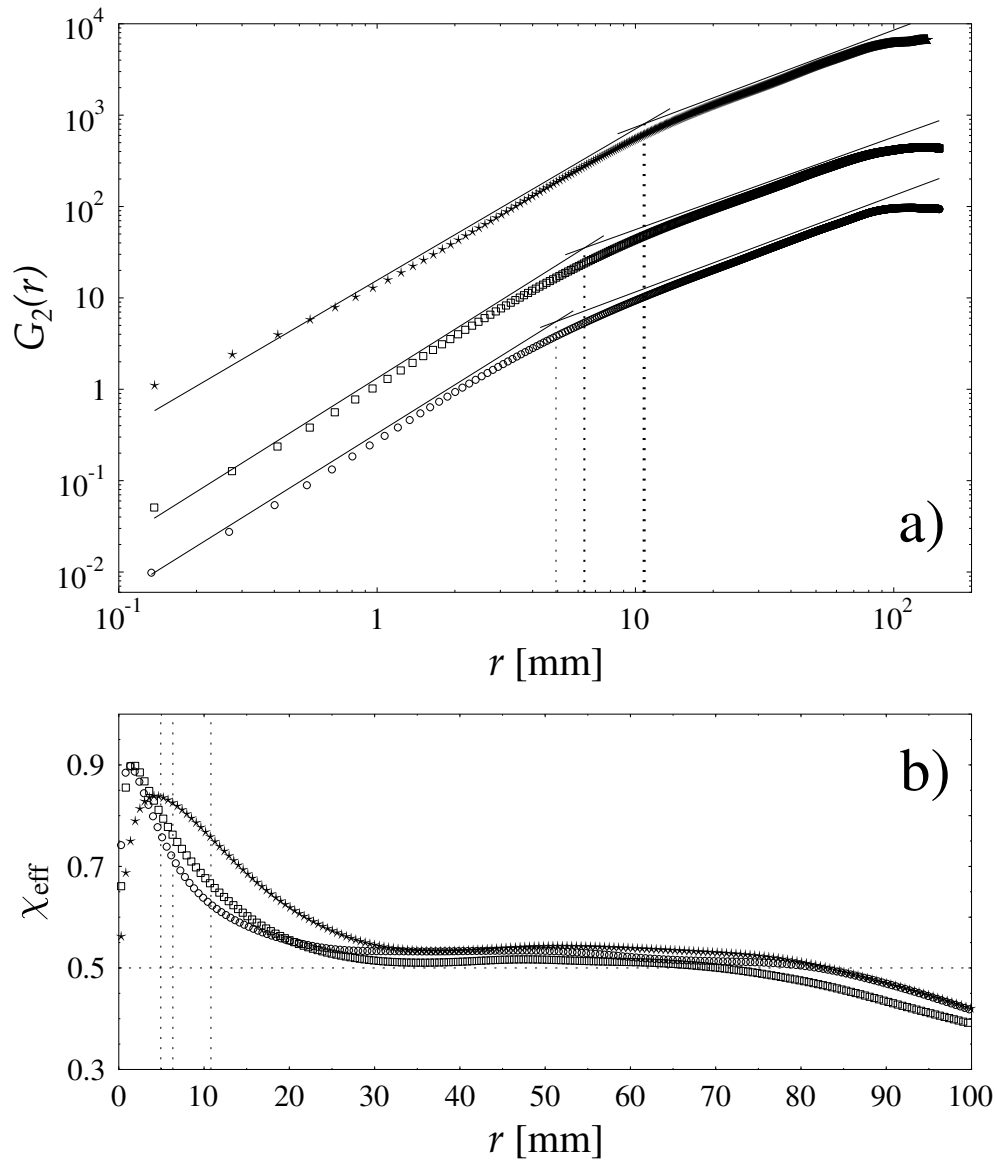
FIGURE 4.2 (a) Spatial correlation functions $G_2(r)$ for three paper grades, and (b) the resulting effective exponents. Crossover scales from the short-range regimes to the asymptotic scaling regimes are marked with dotted lines.

FIGURE 4.3 (a) Temporal correlation functions $C_2(t)$ for three paper grades, and (b) the resulting effective exponents. Crossover scales from the short-range regimes to the asymptotic scaling regimes are marked with dotted lines.
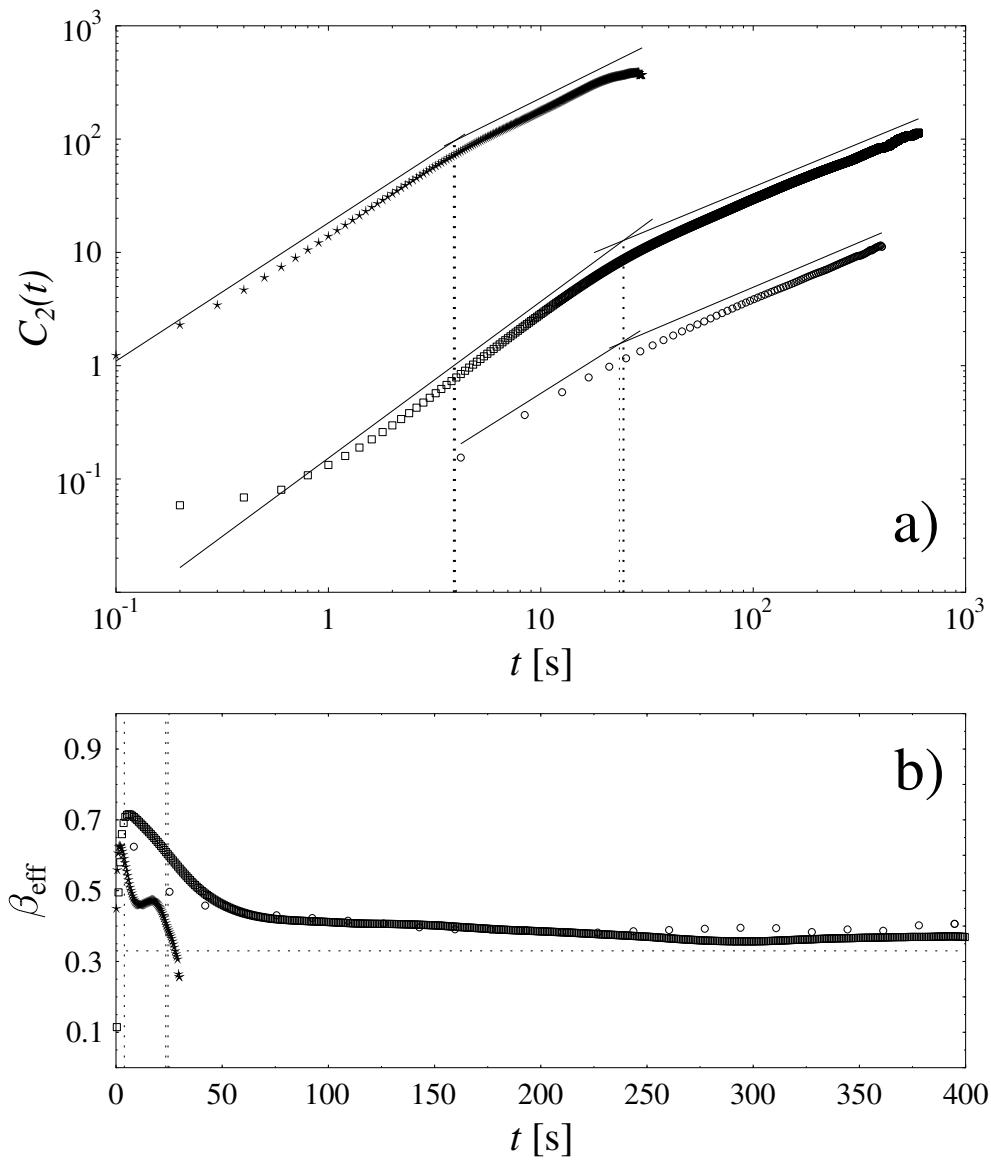
inhomogeneities of the samples. Therefore, we assumed the usual *convolution ansatz* [54, 23, 12], and performed linear least-squares analyses of $\log_{10}[G_q(2r) - G_q(r)] = q\chi \log_{10}(r) + const.$, and of $\log_{10}[C_{s,q}(2t) - C_{s,q}(t)] = q\beta \log_{10}(t) + const.$ The results given in Table 4.1 were obtained after the intrinsic width was subtracted. In log-log plots the short-range regimes seem quite long. Figure 4.2(b), in which the running exponents of $G(r)$ are shown in linear scale, proves however that no well-defined scaling exists in the short-range regime. Also in a semilog plot (not shown) of effective exponents, no evidence of short range scaling can be found. Similar conclusion can be drawn for the temporal correlation function $C_2(t)$ in Figs. 4.3(a),(b). The 'apparent' values of these exponents for short length and time scales were $\chi_{SR} \simeq 0.90$ and $\beta_{SR} \simeq 0.75$, respectively. Especially χ is well above the DPD value for moving fronts, $\chi \approx \beta \approx 0.75$. This indicates that quenched noise in the KPZ equation alone cannot explain the observed short-range behaviour. In the short-range regime the fronts also exhibit apparent multiscaling, *i.e.*, fronts are no longer simply self affine, and have different apparent exponents for different moments in the correlation function Eq.(4.1). The observed multiscaling properties of the fronts are presented in the enclosed Ref. [41]. The short-range behaviour is expected to result from the effective noise at short length scales, and the properties of this noise are studied in Section 4.3. More extensive and precise data analyses for the scaling exponents are presented in the enclosed publications [34, 37, 36, 41, 40].

Another specific property of the KPZ equation is the behaviour of the scaling function $f(t/L^z)$ in Eq. (1.2). In the stationary state KPZ fronts are equivalent to random walks, since a fluctuation-dissipation theorem exists in $1+1$ dimensions [17]. The spatial fluctuations of the fronts depend only on the noise strength D and the surface tension ν, but not on λ. On the other hand, temporal fluctuations at short time scales, and transient phenomena, do depend on the nonlinearity, and thus the crossover function f and its properties are an important indication of KPZ roughening. Likewise one can use to this end the amplitudes of the correlation functions (Eqs. 4.2, 4.3), $A = D/\nu$ and $B = |\lambda|^{2\beta} A^{\beta+1} R_g$, where R_g is a universal constant [13, 22, 38, 21, 11, 45]. The theoretical value of R_g has recently been estimated exactly [45], with the result $R_g = 0.7247031092$. For another universal number in the KPZ theory, the 'strong-coupling fixed point' given by $g^* = 1/2\lambda \left[A/B^{z/2} \right]^{1/\chi}$, the exact [45] result is $g^* \simeq 0.8104567..$, which does not appreciably deviate from the various approximate results that had been achieved earlier [21, 14, 11, 27, 1]. Notice that in this case of $(1+1)$ dimensions, the two universal numbers are not independent, $2g^* = R_g^{-3/2}$. Experimental values for both universal numbers are shown in Table 4.1.

TABLE 4.1 Results for the scaling exponents, amplitudes and universal constants. The two latter quantities were determined for $\beta = 1/3$ and $\chi = 1/2$. The scaling exponents β and χ were obtained by first subtracting the intrinsic widths from the data.

	χ_{SR}	χ_{LR}	β_{SR}	β_{LR}	A	B	R_g	g^*
70 g/m²	0.90(3)	0.50(4)		0.36(3)	0.52(2)	0.186(12)	0.74(6)	0.79(9)
80 g/m²	0.90(4)	0.47(4)	0.75(5)	0.34(4)	0.475(7)	0.14(1)	0.73(5)	0.76(8)
9.1 g/m²	0.85(1)	0.50(6)	0.64(3)	0.43(6)	3.4(1)	8.0(8)	0.62(8)	1.0(2)

In addition to the asymptotic scaling exponents, the universal coupling constant g^* and the universal amplitude ratio R_g were found to be consistent with KPZ behaviour, especially for the two copier papers (80 g/m² and 70 g/m²). For the lens paper agreement was not so good as the shortness of the saturated regime did not allow adequate averaging. A detailed discussion of the universal coupling constant and the universal amplitude ratio is presented in the enclosed publication [40]. For the copier papers in particular, the measured values are indeed very close to the exact results quoted above.

4.2 Demonstrating the existence of the nonlinear term

The different terms in the KPZ equation Eq. (1.4) have a physical meaning and their coefficients can be determined from the recorded fronts. The nonlinear term, for example, arises from propagation in the direction of the local outward normal of the front, and the coefficient λ can thus be determined from the dependence of the local velocity on the local slope. In a KPZ system the velocity v of a segment of length ℓ is $v = v_0 + (\lambda/\ell) \int_0^\ell dx \sqrt{1 + (\nabla h)^2}$. If the local slopes of the front are small, the slope (m) dependent velocity can be expressed in the form $v(m) \approx c + (\lambda/2)m^2$, when only the highest-order term from the expansion of the square-root term is included [17]. The values determined for λ were 0.37(3) and 5.1(2) mm/s for the copier- and lens-paper fronts, respectively, determined for a length scale of ℓ=10 mm.

Another way to study effects of various terms in the (presumably KPZ type) evolution equation is to use a specifically prepared sample. The existence of the nonlinear term can be demonstrated, and the value of λ estimated, from the effect a columnar defect has on the front profile as suggested by Wolf and Tang [55]. Based on a mean-field calculation, and simulations on a lattice model that belongs to the KPZ universality class, they concluded that the effect of the nonlinear term can be seen from the difference in the front profile between defects with a higher and correspondingly lower front velocity in the defect. Despite of its apparent simplicity, this kind of experiment has never been performed before. This may be due to the
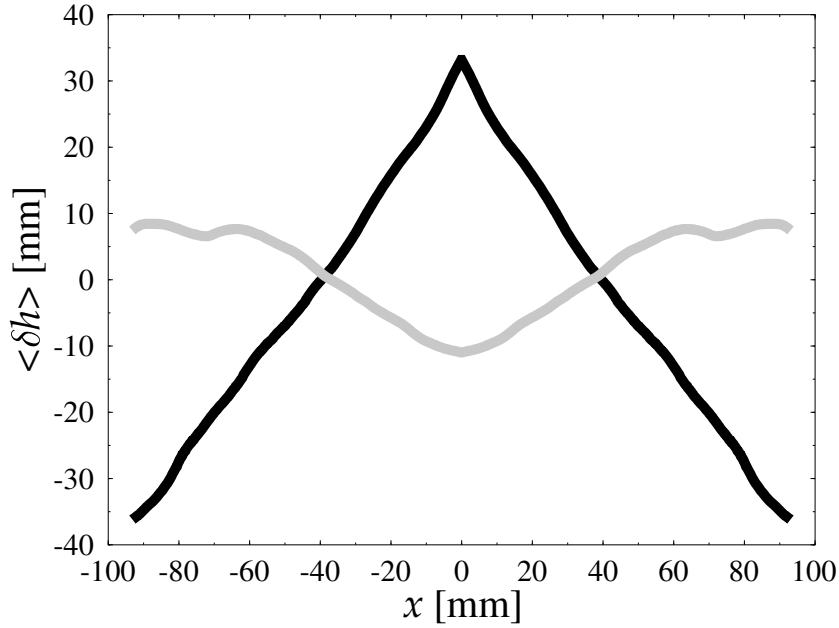
FIGURE 4.4 Averaged front profiles for an advancing and a retarding defect in the middle of the sample, for ΔC = 0.33 g/m^2 (black line) and ΔC = -0.33 g/m^2 (grey line).

fact that it turns out to be rather difficult to perform such an experiment (both cases included) in a controlled way.

In this experiment we used lens paper of size (200×550) mm^2 and the columnar defect was a 10 mm wide stripe in the middle of the sample. The velocity of slow-combustion fronts was again controlled by varying the KNO$_3$ concentration. The front velocity in lens paper is shown in Fig. 4.8 a) as a function of KNO$_3$ concentration. The samples were prepared by spraying KNO$_3$ first to the area of the lower concentration, which was then masked and another spraying was done to get a higher amount of KNO$_3$ in the remaining part of the sample. The amount of the applied KNO$_3$ was measured as described in Chapter 3. The control parameter of the problem is the difference in the KNO$_3$ concentration between the columnar defect (C) and the rest of the sample (C_0), $\Delta C \equiv C - C_0$.

According to the mean-field solution of Wolf and Tang, for a positive coefficient of the nonlinear term (applicable for smouldering fronts), the propagating fronts should asymptotically assume a forward pointing triangular shape (amplitude ΔH_+) around an advancing (faster front velocity, $\Delta C > 0$) defect. In the case of a retarding defect ($\Delta C > 0$), the sides of the stationary profile should not be linear asymptotically, and the amplitude ΔH_- of the deformation should be clearly smaller. This kind of difference between the front amplitudes is clearly seen in Fig. 4.4. For an advancing defect the amplitude of the triangular profile depends on ΔC,
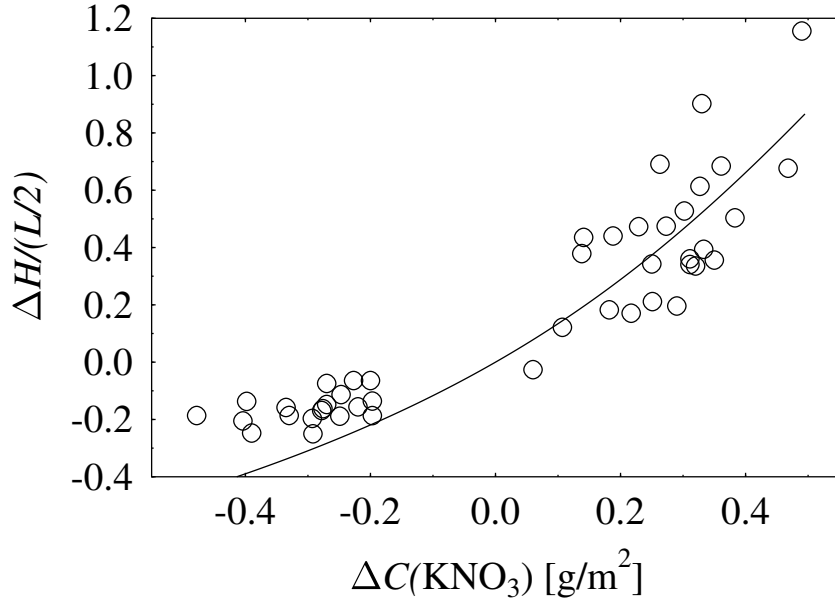
FIGURE 4.5 The absolute value of the amplitude ($\Delta H \equiv |\Delta H_\pm|$) of the deformed front profile around a columnar defect, scaled with $L/2$, as a function of difference in the KNO_3 concentration between the defect and the rest of the sample (o). The full line is a fit by the mean-field solution.

system size L, coefficient of the nonlinear term λ and an effective ('renormalized' by noise induced fluctuations) surface tension ν_e. By fitting our data of 44 burns with the mean-field solution as a function of ΔC, see Fig. 4.5, we found that $\nu_e \simeq 144$ mm^2/s and $\lambda \simeq 5.6$ mm/s. In these estimates we have used an 'effective' sample width $L_{\text{eff}} \simeq 180$ mm, smaller than the 202 mm of the actual sample due to the width of the defect stripe and to allowing for some boundary effects. It is evident that 'renormalization' of the surface tension is substantial, although it is rather difficult to estimate the value of the 'bare' surface tension because of other 'renormalization' effects. The value for λ is a bit higher than those determined by other methods (4.1 - 5.1 mm/s), but is reasonable in view of the rather large fluctuations in the data used here.

In addition to the stationary profiles analysed above, it is possible to study the transient profiles, *i.e.*, how the defect induced profiles grow at the initial phases of the process ($\Delta H_\pm(t)$). The transient behaviour of the profile around an advancing column is particularly simple. The Burgers equation (mean-field solution) admits, [55] in this case a solution of exactly the same shape as the stationary solution, which grows linearly in time until its baseline reaches the width of the sample. Such a 'self-similar' transient does not exist in the case of negative ΔC, so analytical results for transient behaviour are then difficult to find. We found that the initial transient behaviour was clearly linear in time especially for $\Delta C > 0$. In this case the trend
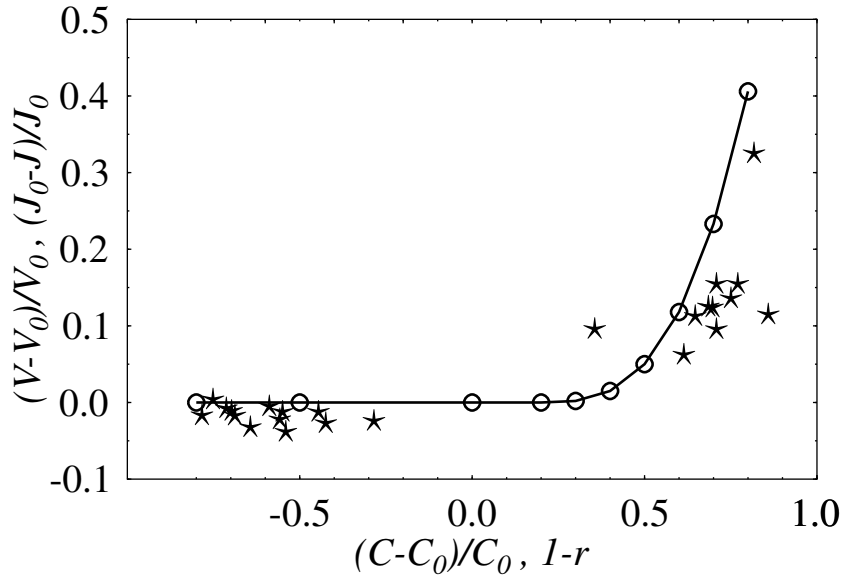
FIGURE 4.6 Scaled velocity change of slow-combustion fronts due to a columnar defect as a function of $(C - C_0)/C_0$ ($\star$), and scaled current change in the totally asymmetric ASEP model due to a defect bond as a function of $(p - rp)/p = 1 - r$ ($\circ$). The full line connects the latter data points. $V_0(J_0)$ is the average velocity (current) without the defect column (bond).

continued nearly linear until the baseline of the defect profile reached the sample size L. For $\Delta C < 0$ the behaviour was quite similar except that saturation took place earlier. There was also some indication that in this case the growth of ΔH_- became nonlinear in time already before saturation, but because of the large fluctuations in the velocity of the smouldering fronts in lens paper, it was difficult to determine the detailed behaviour for small negative concentration differences ΔC. We expect that the nearly linear behaviour initially of ΔH_- is due to the system not being in a fully asymptotic regime.

According to the mean-field solution an advancing defect causes a net increase in the interface velocity, while there is no effect in the infinite size limit in the case of a retarding defect. By this theory a transition in the average interface velocity thus occurs at zero concentration difference, *i.e.*, $\Delta C_{\rm cr} = 0$. There is a related phase change in the shape of the interface: it is faceted for $\Delta C > 0$, and rounded (flat in the thermodynamic limit) for $\Delta C < 0$. This faceting transition can be analysed in more detail by mapping the problem to a totally asymmetric exclusion process with a fast or slow bond in the middle of the system [25]. This model describes particles hopping with a rate p to the next lattice site on the right *(e.g.)*, except for the defect bond where the hopping rate is rp. Free boundaries correspond to the experimental system used for slow-combustion fronts. This problem admits an accurate numerical solution for the effect on the average current (J) (average front velocity (V)) of a

defect bond. The results of the numerical solution of this model together with experimental results for slow-combustion fronts in paper, shown in Fig. 4.6, indicate that the expected transition indeed appears but at a non-zero positive value $\Delta C_{\mathrm{cr}} > 0$. The numerical results indicate that the transition is continuous, and that there is a deformation of power-law type in the faceted interface profile near the defect, but so far the experimental accuracy has not allowed us to accurately characterize these predictions.

The strength of the surface tension term was also tested by igniting fronts with a sine-wave initial conditions with different wave numbers. The decay rate of the amplitudes should be proportional to the surface tension ν. Because of time-consuming sample preparation, this approach was only tested, and the results have not yet been published. With some extra effort, it seems to be possible to get another independent estimate for ν with this set-up. With the limited statistics so far, only an order of magnitude estimate was possible.

4.3   Effective noise

As already discussed above, an evolution equation appropriate for the description of the dynamics of slow-combustion fronts includes a noise term η, which takes care of the fluctuating forces that affect the front propagation, and has been suspected to be responsible for the anomalous short-range behaviour of the fronts. The effective noise η_{eff} can be assumed to be well approximated by the velocity fluctuations of the fronts in the steady-state regime [18]. Equivalently one can consider the velocity fluctuations scaled by the time difference used to define the velocity, *i.e.*, the height fluctuations

$$\eta_{\mathrm{eff}}(x,t) \equiv \delta h(x, t + \tau) - \delta h(x,t), \tag{4.4}$$

where $\delta h(x,t) = h(x,t) - \overline{h}(t)$. The noise amplitude distributions defined in this way for time steps below and above the crossover time scale (3.7 s) for lens paper are shown in Fig. 4.7. For short time steps the distributions show a power-law tail of the form $P(\eta_{\mathrm{eff}}) = c\eta_{\mathrm{eff}}^{-(\mu+1)}$, with $\mu \simeq 1.7$. For higher τ the power-law tail of $P(\eta_{\mathrm{eff}})$ becomes less visible, the exponent μ increases towards $\mu = 5$, and the distribution approaches a Gaussian. Results for both copier papers showed a similar vanishing power-law tail for increasing time difference in the noise amplitudes $P(\eta_{\mathrm{eff}})$ [40].

Correlations in the effective noise were studied by using the two-point correlation function of the velocity fluctuations,

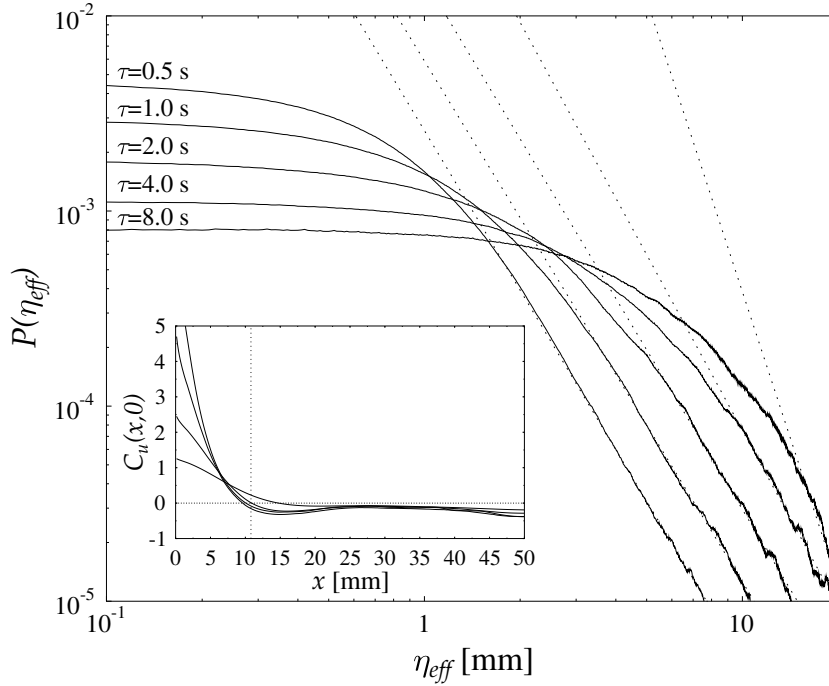$$C_u(x,t) = \langle \delta u(x_0 + x, t_0 + t) \delta u(x_0, t_0) \rangle, \tag{4.5}$$

FIGURE 4.7 The noise amplitude distribution $P(\eta_{\text{eff}})$ for slow-combustion fronts in lens paper determined for time steps $\tau = 0.5, 1.0, 2.0, 4.0$, and 8.0 s. The inset shows the spatial correlations of the velocity fluctuations in the same samples.

with $\delta u(x,t) = u(x,t) - \overline{u}(t)$, and $u(x,t) = [h(x,t+\tau) - h(x,t)]/\tau$. The spatial correlations for lens paper are shown in the inset of Fig. 4.7. Correlations for all time steps τ decay at about the crossover scale found from the correlation function $G(r)$. The effective noise $\eta_{\text{eff}}(x,t)$ has a power-law distributed amplitude and is correlated in the range where anomalous apparent exponents were found, and becomes Gaussian white noise above the crossover scales where KPZ scaling was found. Non-Gaussian amplitude distribution and correlations are both expected to affect the apparent scaling exponents, so we expect these features of noise to explain the observed short-range behaviour of smouldering fronts.

4.4 Determination of KPZ parameters by an inverse method

The existence of the nonlinear and surface tension terms in the evolution equation for smouldering fronts is evident from the experimental results described above, and the scaling properties and the other observed features of these fronts also show them to asymptotically obey the KPZ dynamics. Nevertheless, it is instructive to determine the coefficients of KPZ equation directly from the space- and time-dependent

fronts, and to this end we used the inverse method introduced by Lam and Sander [28]. In this method the coefficients of the discretized KPZ equation are calculated as functions of coarse graining. The continuum KPZ equation (Eq. 1.4) is discretized such that

$$\frac{\Delta h_i(t)}{\tau} \simeq \mathbf{a} \cdot \mathbf{H}_i(t) + \eta_i(t), \qquad (4.6)$$

where τ is the discretization time step (a multiple of the recording time step), $\mathbf{a}$ is a vector of the coefficients of the KPZ equation $\mathbf{a} = [c, \nu, \lambda/2]$, the vector $\mathbf{H}_i(t) = [1, \nabla^2 h, (\nabla h)^2]$ contains the coarse-grained derivatives of the surface height, and $\eta_i(t)$ is here assumed to be Gaussian white noise. Spatial coarse graining is done by truncating the Fourier components with wavelengths smaller than ℓ for the recorded front heights $h(x, t)$. The vector $\mathbf{H}_i(t)$ is calculated from the coarse-grained front heights for different time steps τ, and the vector of the coefficients $\mathbf{a}$ is determined by minimizing the function $\mathcal{J}(\mathbf{a}) = \langle [\Delta h_i(t)/\tau - \mathbf{a} \cdot \mathbf{H}_i(t)]^2 \rangle_{i,t}$. The noise correlator D is determined from the relation $D = (\ell \tau/2) \mathcal{J}(\mathbf{a}_{min})$ with $\mathbf{a}_{min}$ the solution of the minimizing problem. The 'measured' values for the coefficients for a copier paper (80 g/m^2) and the lens paper are given in Table 4.4. The renormalization of the co-efficients as function of the coarse graining parameters τ and ℓ for lens paper is shown in Fig. 5.1. The quoted values are averages over coarse-graining lengths $\ell \in [15,20]$ mm, and determined for the longest coarse-graining times τ used. For c and λ, smaller values for τ can, and have been, used in Ref. [35]. The consistency

Paper grade	c [mm/s]	λ [mm/s]	$\nu(\frac{\tau}{\Delta t})^{-1/3}$ [mm^2/s]	D/ν [mm]
Copier paper	0.49(2)	0.40(2)	0.49(3)	0.83(5)
Lens paper	9.2(5)	4.1(2)	2.0(1)	4.6(11)

TABLE 4.2 Measured values of the coefficients for a copier paper and the lens paper.

of the inverse-method results was tested with direct numerical simulations of the KPZ equation to be described in the next Chapter 5. For better numerical accuracy of the results a new robust filtering method was also used to remove erratic features (effects of sparks) in the recorded front lines [35]. A more complete description of the inverse method and its results are given in the Thesis of Jussi Maunuksela [33] and in the enclosed publications [42,35].

4.5 Pinning transition and avalanches

For untreated paper samples the velocity of the propagating slow-combustion fronts would in principle depend on the properties of the paper, (i.e.), its density, moisture and the amount and type of fillers, if they would propagate. Cellulose fibres have
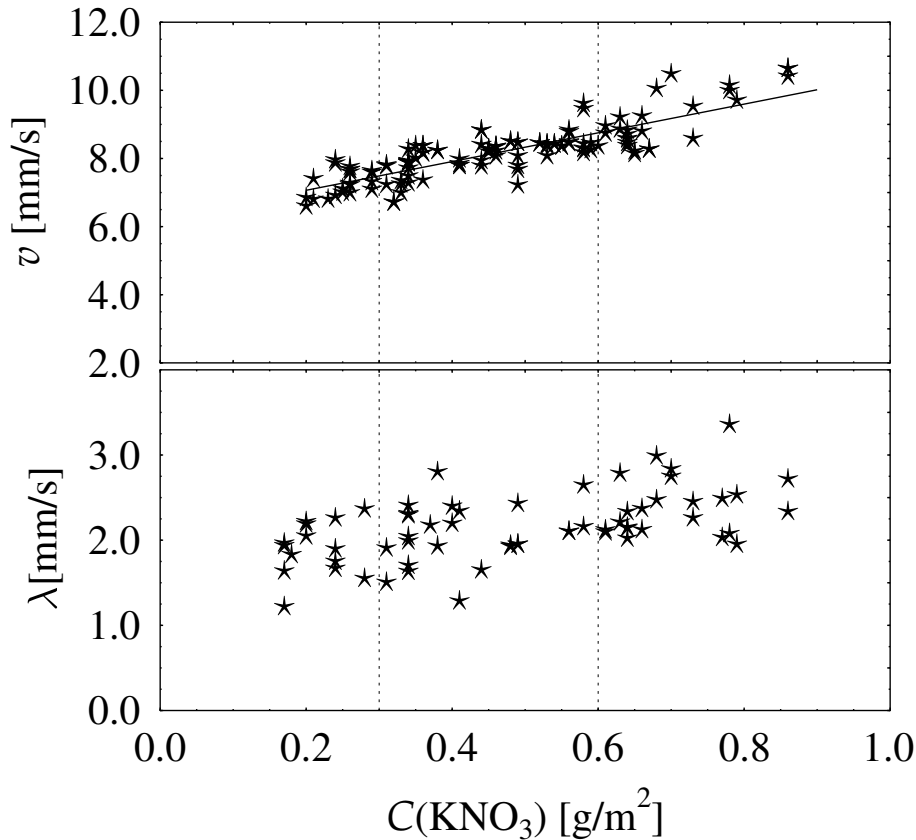
FIGURE 4.8 Velocity v and λ for lens-paper fronts as functions of the KNO_3 concentration. The 'well-propagating' regime in the concentration is denoted by the dotted lines.

such a low conductivity of heat with respect to the amount of heat produced in the slow-combustion process that the latter process cannot sustain propagating fronts. The heat produced per unit time can however be increased by providing additional oxygen, so that eventually slow-combustion fronts do indeed propagate. This additional oxygen we provide with absorbed KNO_3, whose concentration will thus serve as the control parameter of the process. Below a critical value of the KNO_3 concentration (0.15 g/m^2), slow-combustion fronts do not propagate, and slightly above this value a few separated segments of the fronts can propagate for a while until they eventually die out. Examples of quenched fronts are shown in Chapter 6, Fig. 6.1. Even a small further addition of KNO_3 produces then an unbroken propagating front, and this kind of 'well-propagating' fronts with concentrations of (0.36-0.65) g/m^2 were used in the analyses reported above and in the enclosed publications. Increasing still further the amount of KNO_3 will produce avalanche type behaviour in the propagating fronts, until after some value of the KNO_3 concentration, the paper will burst into flames. The velocity of fronts in lens paper samples is presented in Fig. 4.8 as a function of the KNO_3 concentration. When the average front ve-

locity approaches zero, KPZ type models can be divided into different universality classes depending on the behaviour of the coefficient λ of the nonlinear term. For anisotropic models, like directed percolation depinning (DPD), λ diverges when the reduced force $f = (F - F_c)/F_c$ approaches zero. For isotropic models λ vanishes in this limit [52]. As seen from Fig. 4.8, λ more likely decreases than diverges as the front velocity, or the KNO_3 concentration, decreases. Moreover, the scaling exponents ($\chi \approx \beta \approx 0.75$) for the DPD model in the case of moving fronts differ from the exponents measured here. To obtain more reliable data in the presence of pinning, the front detection algorithm and the analysis software should however be modified.

For higher KNO_3 concentrations occasional avalanches evolve, typically in the centimetre range. If a relatively large forward fluctuation appears in the front, a nonlinear term of KPZ type will spread the defect in the lateral direction as seen in Fig. 4.9. These moving 'kinks' appear as local avalanches in the fronts, and obviously give rise to apparent multiscaling [6]. Areas of fronts with steep slope are increasingly magnified by increasing the power of the correlation function. The effect of the avalanches was tested by calculating qth order correlation functions (Eq. 4.2 and Eq. 4.3) for different sets of burns depending on the abundance of avalanches. It was evident that multiscaling was more pronounced when there were more avalanches present.

To conclude, our results indicate a clear asymptotic scaling behaviour of the KPZ universality class. This is evident from the asymptotic behaviour of the spatial and the temporal qth order correlation functions (Eqs. 4.3 and 4.2), and from the scaling exponents determined from the local width. In addition to the KPZ scaling exponents, we found consistent values for the universal coupling constant g^* and for the universal amplitude ratio R_g. We also have demonstrated the existence of the nonlinear term from the propagating fronts and determined coefficients of the KPZ equation by an inverse method [28]. For short temporal and spatial scales we find higher apparent scaling exponents with apparent multiscaling. We also find that the effective noise $\eta_{\text{eff}}(x, t)$ is both correlated and power law distributed below the crossover scales, which explains the observed non-trivial scaling behaviour.
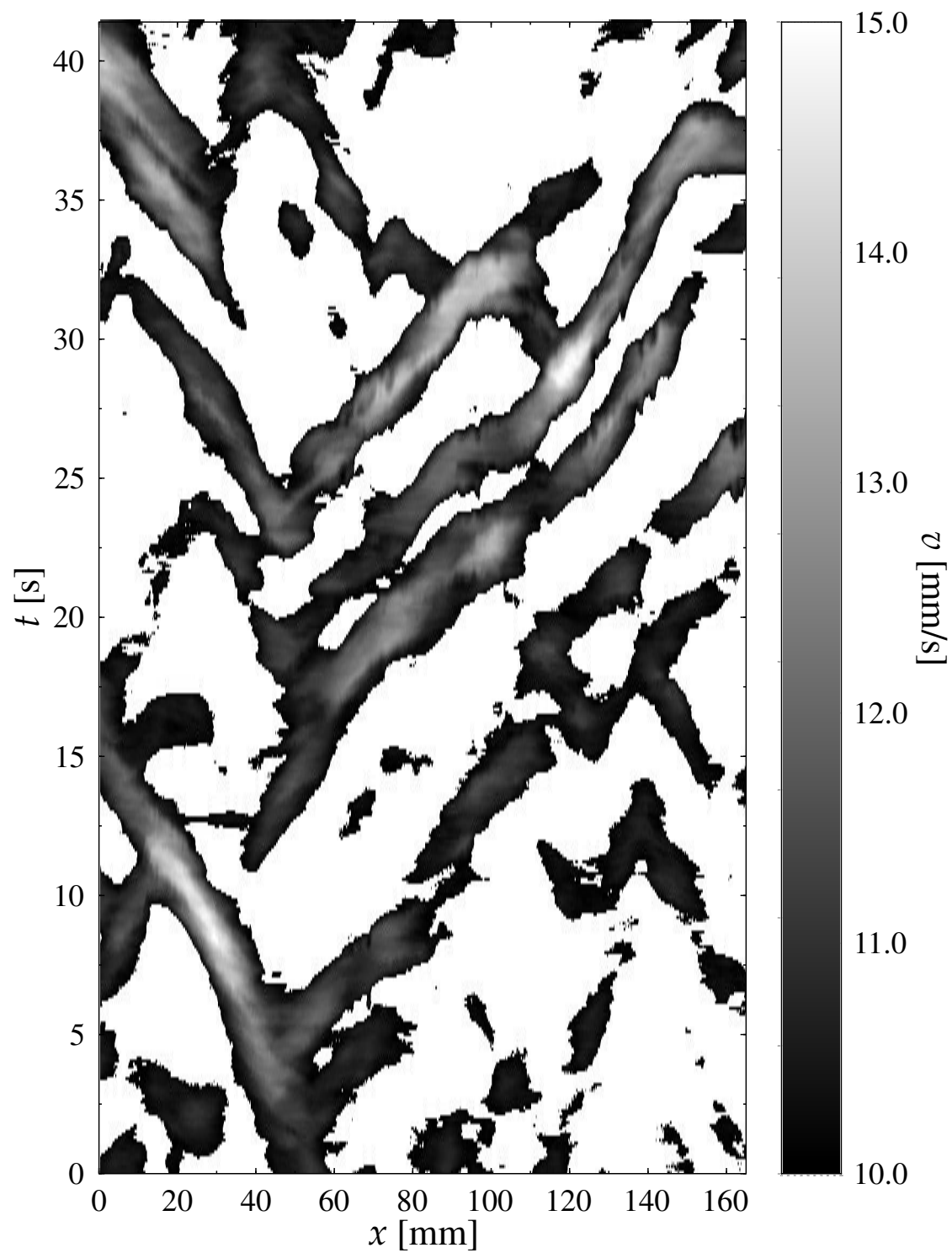
FIGURE 4.9 Map of the highest local velocities (avalanches) for a single lens paper burn with a KNO_3 concentration of 0.7 g/m^2. White areas in the figure correspond to velocities below the average velocity (v_{ave}=10 mm/s).

Chapter 5

Numerical solution of the KPZ equation

Numerical work on interfaces has often been focussed on the asymptotic behaviour of driven interfaces with uncorrelated Gaussian (white) noise, but experimental systems are always restricted in size and often dominated by anomalous noise. Therefore, we used direct numerical solution of the KPZ equation with real noise to understand the short-range behaviour observed in our experiments. The noise was obtained from real paper samples and it thus included inherent correlations. We concentrate here on the connection between the experimental (the main focus of this Thesis) system and the simulations. A more detailed account of the results of the numerical work can be found in the enclosed publication [42].

The numerical solution of the KPZ equation (Eq. 1.4) was achieved by using the Euler's method solution of the finite difference equation

$$h_i^{n+1} = h_i^n + \frac{\Delta t}{\Delta x^2}\Big[\nu_0(h_{i+1}^n + h_{i-1}^n - 2h_i^n) + (\lambda_0/6)[(h_{i+1}^n - h_i^n)^2$$

$$+(h_{i+1}^n - h_i^n)(h_i^n - h_{i-1}^n) + (h_i^n - h_{i-1}^n)^2]\Big] + \Delta t\, c_0 + \sqrt{\frac{2D_0\Delta t}{\Delta x}}\, \xi(i, h_i^n), \qquad (5.1)$$

where h_i^n is the front position $h(x_i, t_n)$ at the i'th lattice point at the n'th time step. The nominal values of the parameters ν_0 and λ_0 were obtained by an inverse method [33] from our experimental data as described above. The effective values of the KPZ parameters for the experimental data and for the 'best simulation model' are shown in Fig. 5.1. For the lens paper ν_0=5 mm^3/s and λ_0=2 mm/s, and for both copier papers ν_0=0.10 mm^3/s and λ_0=0.3 mm/s, were thus used. The nominal values for c_0 and D_0 were fixed by comparing the velocity distributions from simulations and experiments.
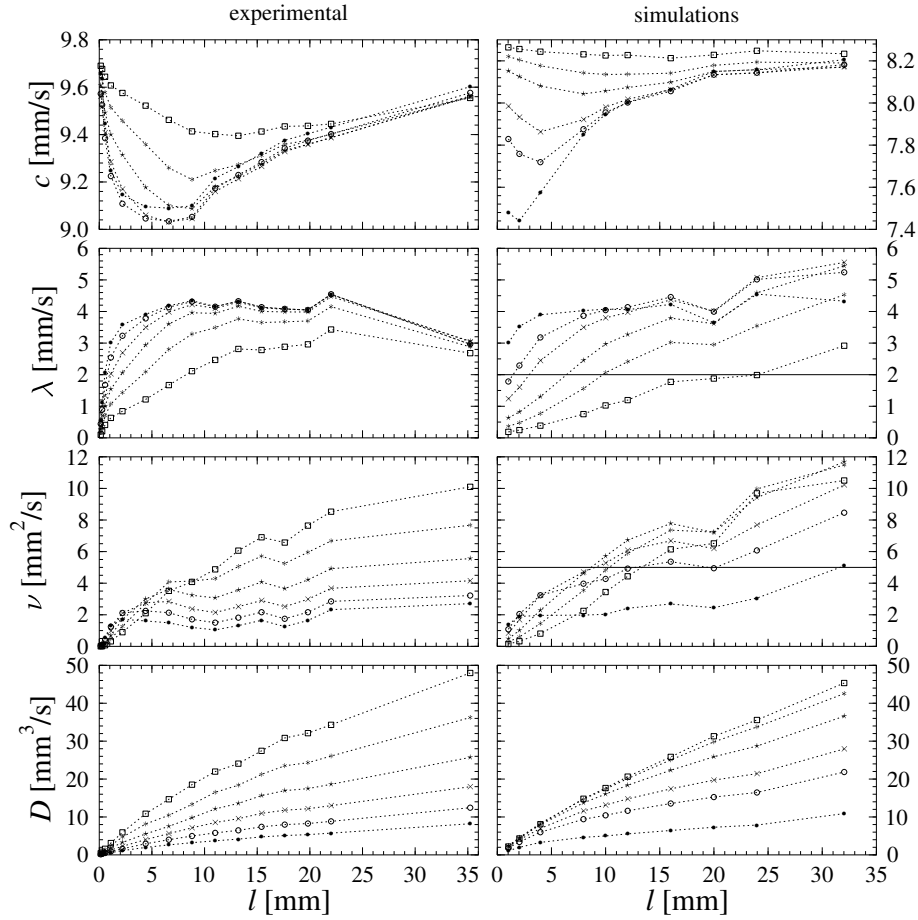
FIGURE 5.1 The effective parameters for $\tau = 0.2(.)$, $0.4(\circ)$, $0.8(\times)$, $1.6(\star)$, $3.2(*)$ and $6.4(\square)$ s of the KPZ equation as determined by the inverse method. On the left are the experimental values and on the right the effective values determined from the simulated fronts produced by our 'best simulation model'. The nominal values λ_0 and ν_0 are indicated by the horizontal lines.

The two-dimensional noise matrices $\xi(i, h_i^n)$ were obtained from β-radiographs of copier papers (two samples of 70 g/m^2 and three samples of 80 g/m^2), and from ten scanned images of lens paper (Fig. 3.1). A set of simulations was also done with uncorrelated noise generated by disordering the pixels in the scanned images of lens paper, *i.e.*, by scrambling that noise. This scrambled noise was used as both quenched and annealed noise in Eq. 5.1. In the simulation the value of the noise for a given, not discrete, value of h_i^n, was obtained from the noise matrix $\xi(i, h_i^n)$ as a linear extrapolation, except in the case of annealed noise when the noise matrix was scrambled at every simulation step. For the nonlinear term we used an improved discretization introduced by Lam and Shin [29] to produce the correct renormalization of the KPZ parameters under coarse graining. To model the experiments, free boundary conditions were naturally used, but we also studied possible effects of pe-

riodic boundary conditions. The spatial resolution Δx of the simulations was set to be the same as the resolution in our experiments, Δx =0.102 mm. The temporal resolution Δt was set small enough to ensure the numerical accuracy of the integration. For too small values of Δt the simulated fronts reached a pinned, not propagating, configuration of $h(x,t)$, where the deterministic terms of Eq. (5.1) and the noise contribution locally had exactly opposite values. This happens because for increasing the temporal resolution Δt the noise term vanishes more slowly than *e.g.* the driving force c_0. For the value Δt=0.001 pinning was observed for $c_0 \simeq 4.5$, which was well below the value $c_0 \simeq 10$ used in our 'best simulation model'.

We also tested other possible discretizations of the nonlinear term. The most simple version was the standard discretization $\frac{\Delta t}{\Delta x^2}(\lambda_0/8)(h_{i+1}^n + h_{i-1}^n)^2$ [39]. We also tested nonlinearity without the small-slope approximation, *i.e.*, the nonlinear term above was replaced by $\lambda_0 \Delta t \sqrt{1 + (h_{i+1}^n + h_{i-1}^n)^2/4\Delta x^2} - \lambda_0 \Delta t$, where the last term is needed to compensate for the exclusion of the constant term in the Taylor expansion of $\sqrt{1 + (dh/dx)^2}$ in Eq. (1.4). In our simulations (with rather limited statistics because of the availability of input noise data) we found no noticeable differences between results produced by different discretizations, or by different boundary conditions.

A data analysis similar to the one of our experimental results was then performed for all simulation data. Unlike in the case of experimental data, there was no reason to remove a global tilt from the fronts because scanner errors were corrected by normalizing the average of each column of the noise matrices to zero. The evolution of the front width in the lens-paper simulations is shown in Fig. 5.2. The solid line denotes the front width $w^2(t)$ averaged over ten independent simulations starting from flat initial conditions. The dashed line is the evolution of ten simulations with the same noise but with different rough initial conditions. The guideline in Fig. 5.2 corresponds to the theoretical value for the growth exponent in the asymptotic regime, $\beta = 1/3$. The inset shows the magnitude of the fluctuations for ten independent simulations.

In Fig. 5.3(a) we show the spatial correlation function $G(r)$ for simulations, where as the input noise we used an optically scanned image of lens paper [denoted by (I)], β- radiographs of copier papers [(II) and (III)], disordered annealed [A(IV)] and quenched [Q(IV)] noise (with the amplitude distribution of the lens paper) . Like in the experiments (see Figs. 4.2, 4.3), distinct crossovers to asymptotic scaling are evident, except in the result for noise A(IV). The slopes of the guidelines in the figure are taken from the experimental results and match well the simulated results. For the short-range regime we find $\chi_{SR} \sim 0.9$ and for the long-range (asymptotic) regime $\chi_{LR} \sim 0.5$. We note that $G(r)$ displays quite a short asymptotic scaling
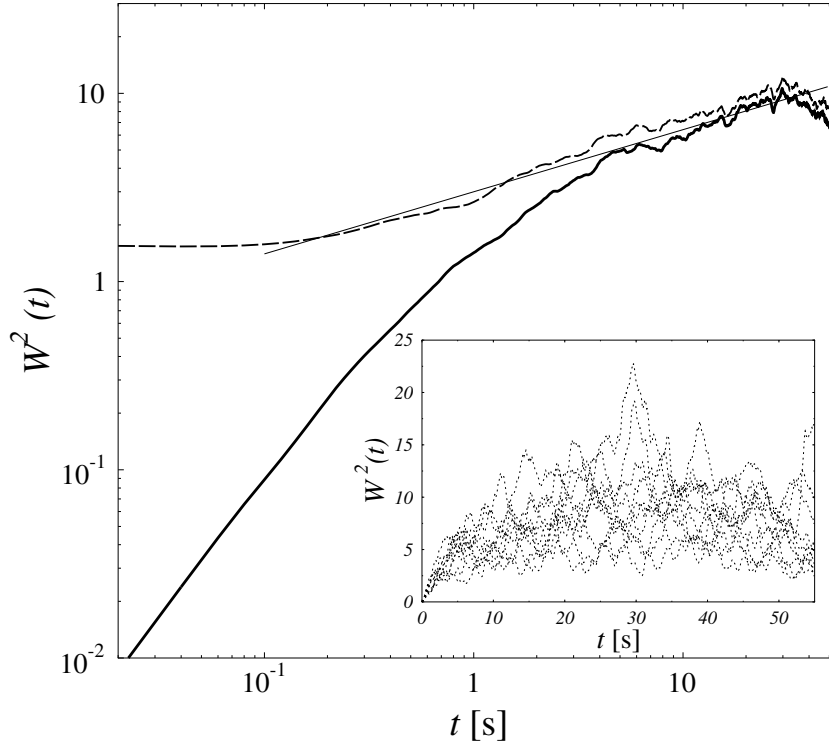
FIGURE 5.2 The average front widths w^2 as functions of time for ten lens-paper simulations. The result for a flat initial condition is plotted with a thick solid line, and with a dashed line for rough initial conditions. The inset displays the magnitude of fluctuations, showing the individual results for ten realizations of noise.

regime if the simulations are started from flat initial conditions. This is because of the limited size of the 'paper' (scanned noise matrix) in the simulations. Increasing the nonlinearity and starting from a rough initial configuration speeds up roughening, and facilitates a more accurate determination for χ_{LR}. The temporal correlation functions $C(t)$ for the same simulations are shown in Fig.5.3(b). Again, the slopes of the guidelines are taken from experiments [40], and correspond to $\beta_{\mathrm{SR}} = 0.7$ and $\beta_{\mathrm{LR}} = 0.33$. Like in the experimental results, the short range 'apparent' roughness exponent exponent is above the reported DPD value [17]. In Table 2 of Article VI we show the locations of the crossover points r_c and t_c for spatial and temporal correlation functions, respectively. First, the values r_c and t_c produced by the simulation models are reasonably close to those measured in the experiments [40]. As expected, simulations with randomized annealed noise A(IV), display no crossover, and for randomized but quenched noise Q(IV), crossover-like behaviour occurs only at a scale of a few discretization steps. The second question concerns the origin of the crossovers. By comparing different simulations we observe that, for the given noise correlations, the spatial crossover scale r_c is not very strongly dependent on the simulation parameters or on $\langle v \rangle$. We conclude that r_c is mainly determined by
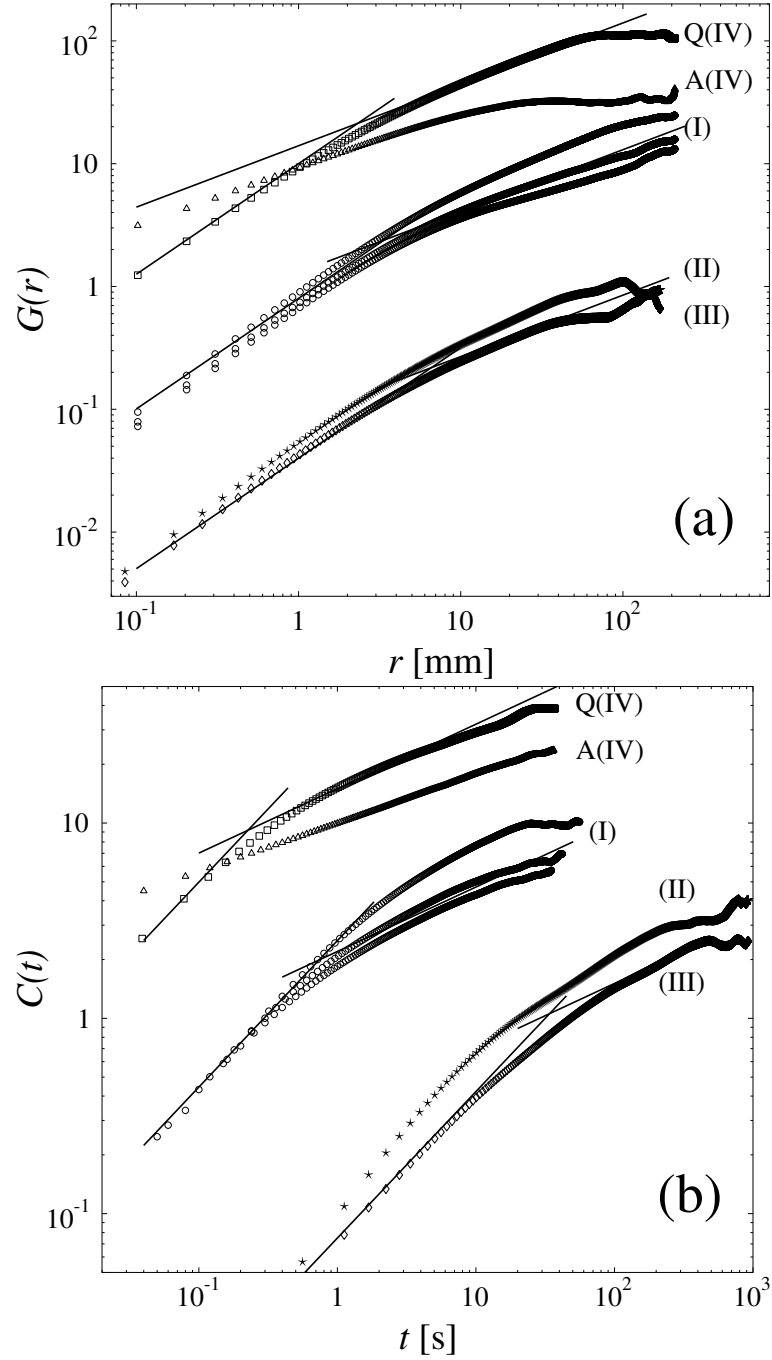
FIGURE 5.3 (a) Correlation functions $G(r)$ for five different noises (see text). The solid lines correspond to the experimentally observed scaling exponents (χ_{SR}=0.9 and χ_{LR}=0.5). (b) Correlation functions $C(t)$ for the same noises. The solid lines correspond to the experimentally observed scaling exponents (β_{SR}=0.7 and β_{LR}=0.33). For comparison, we whow for lens-paper noise the correlation functions for three different values of the driving velocity, curves from top to bottom have $c_0 = 8.4$, 11.4, and 13.4 mm/s, respectively. Of these $c_0 = 11.4$ mm/s is the 'best simulation model' for the lens paper.
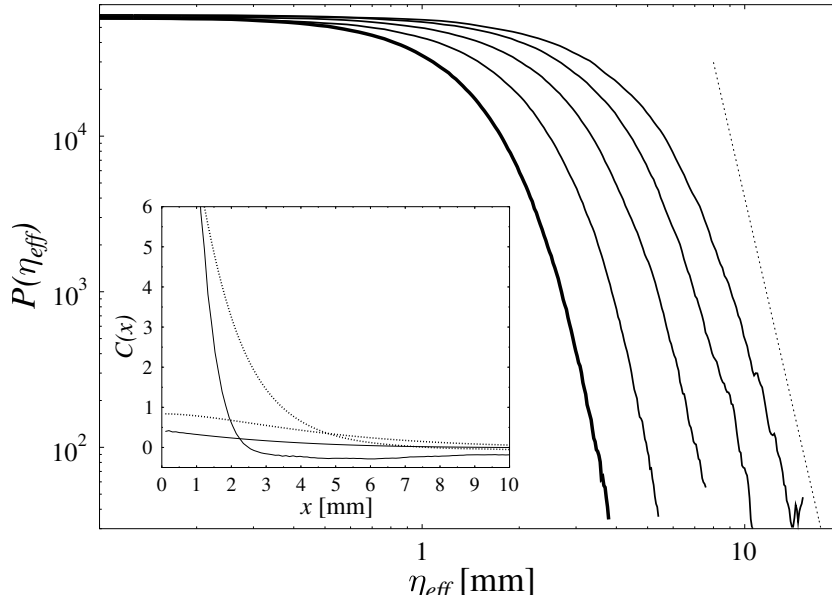
FIGURE 5.4 Amplitude distributions of effective noises as determined for τ= 0.5, 1.0, 2.0, 4.0 and 8.0 s, from left to right, from lens-paper simulations. The slope of the dotted line is −9. The inset shows effective noise correlations from the simulations with real noise (dotted lines) and with randomized noise (solid lines).

the correlations in the input noise. Within the accuracy of the crossover values, we find that $r_c \sim t_c\langle v\rangle$, where the constant of proportionality is close to unity. This result is in agreement with r_c being mainly determined by the input-noise correlations, as asymptotic scaling would in this case be expected for times $t > r_c/\langle v\rangle$.

The effective noise was determined for the simulated fronts exactly as for the experimental data. An interesting feature concerning the effective-noise correlations $C(r)$ becomes evident from the inset of Fig. 5.4, where these correlations for simulations with real and randomized input noise are shown. For both simulations, the effective-noise correlations were rather similar, despite the totally different nature of the input noises. We can conclude that the correlation function $C(r,t)$ calculated from the local velocities, Eq. (4.5), includes a significant contribution from the deterministic part of the dynamics. The amplitude distributions $P(\eta_{\text{eff}})$, shown in Fig. 5.4, of these effective noises had no power-law tails for any time step τ, in contrast with the experimental results of Fig. 4.7, and also no multiscaling was found in the correlation functions $C_q(t)$ and $G_q(r)$. Thus, as expected, the present KPZ simulations can not include all features of the real burning process, *e.g.*, the dynamical features of noise.

Chapter 6

Conclusions

In this Thesis I have presented a detailed description of a high-resolution well-controlled experimental set-up for studies on the dynamics of slow-combustion fronts. Specially prepared paper samples of varying size were 'burned' in the combustion chamber, and the propagation of the smouldering fronts was recorded with high spatial and temporal resolution. Several different measurement configurations were used to obtain more detailed information about the roughening process.

A large amount of data for different paper grades, measured with different set-ups, was carefully analysed, and two separate regimes were found. The asymptotic scaling behaviour of the fronts is clearly that of the KPZ universality class, and their apparent short-range scaling is dominated by nontrivial noise leading to anomalous higher 'effective' exponents and apparent multiscaling. Other proofs of the KPZ universality class were achieved by determining the universal coupling constant and amplitude ratio, by determining the parameters of the applicable KPZ equation, and by studying the first-return probabilities of front fluctuations. The existence of the nonlinear term in the evolution (KPZ) equation was independently shown by analysing the effect of columnar defects on the front profile.

For reliable results we performed extensive averaging of the data and carefully analysed the noise characteristics. Simulations of the KPZ equation confirmed qualitatively that our results for anomalous short-range behaviour can be explained by KPZ-type dynamics with appropriate nontrivial noise. We observed no apparent multiscaling properties in the simulations, most probably because of lack of avalanche-type dynamics as seen in the experiments.

Several questions still remain open and will be subjects of further studies. Our preliminary results for the distribution of height fluctuations display interesting non-trivial properties [44]. Furthermore, there are parts of the phase space of the system which have not been analysed in any detail, like the pinning transition, an example of which is shown in Fig. 6.1. This transition, and how it is approached,
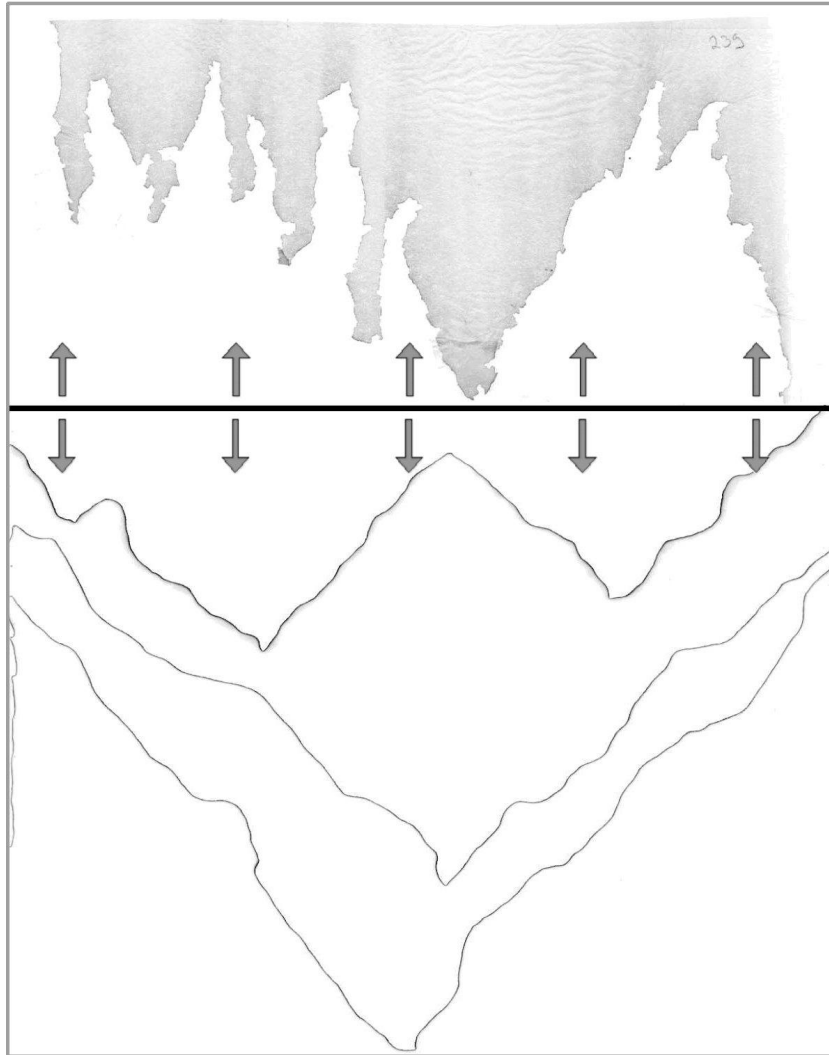
FIGURE 6.1 Pinned interfaces. The lower configurations are for copier paper samples and the uppermost configuration for a lens paper sample with a low KNO_3 concentration.

should be studied in more detail. To conclude, it has been a privilege to work in a challenging field of noisy systems and to see how a process with a large number of parameters and randomness can be described by a relatively simple stochastic evolution equation.

Bibliography

[1] AMAR, J. G. AND FAMILY, F., *Universality in surface growth: Scaling functions and amplitude ratios*. Phys. Rev. A **45** (1992) 5378–5393.

[2] AMARAL, L. A. N., BARABÁSI, A.-L., BULDYREV, S. V., HARRINGTON, S. T., HAVLIN, S., SADR-LAHIJANY, R., AND STANLEY, H. E., *Avalanches and the directed percolation depinning model: Experiments, simulations, and theory*. Phys. Rev. E **51** (1995) 4655–4673.

[3] AMARAL, L. A. N., BARABÁSI, A.-L., MAKSE, H. A., AND STANLEY, H. E., *Scaling properties of driven interface in disordered media*. Phys. Rev. E **52** (1995) 4087–4104.

[4] BAK, P., TANG, C., AND WIESENFELD, K., *Self-organized criticality: An explanation of 1/f noise*. Phys. Rev. Lett. **59** (1987) 381–384.

[5] BALANKIN, A. S. AND MATAMOROS, D. M., *Unconventional anomalous roughening in the slow combustion of paper*. Phil. Mag. Lett. **81** (2001) 495–503.

[6] BARABÁSI, A.-L., BOURBONNAIS, R., JENSEN, M., KERTÉSZ, J., VICSEK, T., AND ZHANG, Y.-C., *Multifractality of growing surfaces*. Phys. Rev. A **45** (1992) R6951–R6954.

[7] BARABÁSI, A.-L. AND STANLEY, H. E., *Fractal Concepts in Surface Growth* (Cambridge University Press, Cambridge, UK, 1995).

[8] CHEN, C.-C. AND DEN NIJS, M., *Interface view of directed sandpile dynamics*. Phys. Rev. E **65** (2002) 031309.

[9] DERRIDA, B. AND LEBOWITZ, J. L., *Exact large deviation function in the asymmetric exclusion process*. Phys. Rev. Lett. **80** (1998) 209–213.

[10] FAMILY, F. AND VICSEK, T., *Scaling of the active zone in the Eden process on percolation networks and the ballistic deposition model*. J. Phys. A **18** (1985) L75–L81.

[11] FOGEDBY, H., *Soliton approach to the noisy Burgers equation: Steepest descent method*. Phys. Rev. E **57** (1998) 4943–4968.

[12] FORREST, B. M. AND TANG, L.-H., *Surface roughening in a hypercube-stacking model*. Phys. Rev. Lett. **64** (1990) 1405–1408.

[13] FORSTER, D., NELSON, D. R., AND STEPHEN, M. J., *Large-distance and long-time properties of a randomly stirred fluid*. Phys. Rev. A **16** (1977) 732–749.

[14] FREY, E., TÄUBER, U. C., AND HWA, T., *Mode-coupling and renormalization group results for the noisy Burgers equation*. Phys. Rev. E **53** (1996) 4424–4438.

[15] GWA, L.-H. AND SPOHN, H., *Six-vertex model, roughened surfaces, and an asymmetric spin Hamiltonian*. Phys. Rev. Lett. **68** (1992) 725–728.

[16] HÄKKÄNEN, H. J. AND KORPPI-TOMMOLA, J. E. I., *UV-laser plasma study of elemental distributions of paper coatings*. Appl. Spectrosc. **49** (1995) 1721–1728.

[17] HALPIN-HEALY, T. AND ZHANG, Y.-C., *Kinetic roughening phenomena, stochastic growth, directed polymers and all that. aspects of multidisciplinary statistical mechanics*. Phys. Rep. **254** (1995) 215–415.

[18] HORVÁTH, V. K., FAMILY, F., AND VICSEK, T., *Anomalous noise distribution of the interface in two-phase fluid flow*. Phys. Rev. Lett. **67** (1991) 3207–3210.

[19] HORVÁTH, V. K., FAMILY, F., AND VICSEK, T., *Dynamic scaling of the interfaces in two-phase viscous flows in porous media*. J. Phys. A **24** (1991) L25–L29.

[20] HORVÁTH, V. K. AND STANLEY, H. E., *Temporal scaling of interfaces propagating in porous media*. Phys. Rev. E **52** (1995) 5166–5169.

[21] HWA, T. AND FREY, E., *Exact scaling function of interface growth dynamics*. Phys. Rev. A **44** (1991) R7873–R7876.

[22] KARDAR, M., PARISI, G., AND ZHANG, Y.-C., *Dynamic scaling of growing interfaces*. Phys. Rev. Lett. **56** (1986) 889–892.

[23] KERTÉSZ, J. AND WOLF, D. E., *Noise reduction in Eden models: II. Surface structure and intrinsic width*. J. Phys. A **21** (1988) 747–761.

[24] KIM, D., *Bethe Ansatz solution for crossover scaling functions of the asymmetric XXZ chain and the Kardar-Parisi-Zhang-type growth model*. Phys. Rev. E **52** (1995) 3512–3524.

[25] KOLOMEISKY, A. B., *Asymmetric simple exclusion model with local inhomogeneity.* J. Phys. A **31** (1998) 1153–1164.

[26] KRUG, J., *Origins of scale invariance in growth processes.* Adv. Phys. **46** (1997) 139–282.

[27] KRUG, J., MEAKIN, P., AND HALPIN-HEALY, T., *Amplitude universality for driven interfaces and directed polymers in random media.* Phys. Rev. A **45** (1992) 638–653.

[28] LAM, C.-H. AND SANDER, L. M., *Inverse method for interface problems.* Phys. Rev. Lett. **71** (1993) 561–564.

[29] LAM, C.-H. AND SHIN, F. G., *Improved discretization of the Kardar-Parisi-Zhang equation.* Phys. Rev. E **58** (1998) 5592–5595.

[30] LESCHHORN, H., *Anisotropic interface depinning: Numerical results.* Phys. Rev. E **54** (1996) 1313–1320.

[31] LESCHHORN, H. AND TANG, L.-H., *Avalanches and correlations in driven interface depinning.* Phys. Rev. E **49** (1994) 1238–1245.

[32] MANDELBROT, B. B., *The Fractal Geometry of Nature* (W. H. Freeman and Co., San Francisco, 1982).

[33] MAUNUKSELA, J., *Scaling and noise in slow combustion of paper,* Ph.D. thesis, University of Jyväskylä (2003).

[34] MAUNUKSELA, J., MYLLYS, M., KÄHKÖNEN, O.-P., TIMONEN, J., PROVATAS, N., ALAVA, M. J., AND ALA-NISSILA, T., *Kinetic roughening in slow combustion of paper.* Phys. Rev. Lett. **79** (1997) 1515–1518.

[35] MAUNUKSELA, J., MYLLYS, M., MERIKOSKI, J., TIMONEN, J., KÄRKKÄINEN, T., WELLING, M. S., AND WIJNGAARDEN, R. J., *Determination of the stochastic evolution equation from noisy experimental data.* Eur. Phys. J. B **33** (2003) 193–202.

[36] MAUNUKSELA, J., MYLLYS, M., TIMONEN, J., ALAVA, M. J., AND ALA-NISSILA, T., *Kardar-Parisi-Zhang scaling in kinetic roughening of fire fronts.* Physica A **266** (1999) 372–376.

[37] MAUNUKSELA, J., MYLLYS, M., TIMONEN, J., KUITTU, M., ALA-NISSILA, T., ALAVA, M. J., AND PROVATAS, N., *Maunuksela et al. reply.* Phys. Rev. Lett. **80** (1998) 5707.

[38] MEDINA, E., HWA, T., KARDAR, M., AND ZHANG, Y.-C., *Burgers equation with correlated noise: Renormalization-group analysis and applications to directed polymers and interface growth*. Phys. Rev. A **39** (1989) 3053–3075.

[39] MOSER, K., KERTÉSZ, J., AND WOLF, D. E., *Numerical solution of the Kardar-Parisi-Zhang equation in one, two and three dimensions*. Physica A **178** (1991) 215–226.

[40] MYLLYS, M., MAUNUKSELA, J., ALAVA, M. J., ALA-NISSILA, T., MERIKOSKI, J., AND TIMONEN, J., *Kinetic roughening in slow combustion of paper*. Phys. Rev. E **64** (2001) 036101.

[41] MYLLYS, M., MAUNUKSELA, J., ALAVA, M. J., ALA-NISSILA, T., AND TIMONEN, J., *Scaling and noise in slow combustion of paper*. Phys. Rev. Lett. **84** (2000) 1946–1949.

[42] MYLLYS, M., MAUNUKSELA, J., MERIKOSKI, J., TIMONEN, J., AND AVIKAINEN, M., *KPZ equation with realistic short-range correlated noise*. Submitted to Eur. Phys. J. B.

[43] OLAMI, Z., PROCACCIA, I., AND ZEITAK, R., *Theory of self-organized depinning*. Phys. Rev. E **49** (1994) 1232–1237.

[44] PRÄHOFER, M. AND SPOHN, H., *Universal distributions for growth processes in 1+1 dimensions and random matrices*. Phys. Rev. Lett. **84** (2000) 4882–4885.

[45] PRÄHOFER, M. AND SPOHN, H., *Scale invariance of the PNG droplet and the Airy process*. J. Stat. Phys. **108** (2002) 1071–1106.

[46] PROVATAS, N., ALA-NISSILA, T., AND ALAVA, M. J., *Growth and structure of random fibre clusters and cluster networks*. Phys. Rev. Lett. **75** (1995) 3556–3559.

[47] PROVATAS, N., ALA-NISSILA, T., GRANT, M., ELDER, K. R., AND PICHÉ, L., *Flame propagation in random media*. Phys. Rev. E **51** (1995) 4232–4236.

[48] PROVATAS, N., ALAVA, M. J., AND ALA-NISSILA, T., *Density correlations in paper*. Phys. Rev. E **54** (1996) R36–R38.

[49] RUBIO, M. A., EDWARDS, C. A., DOUGHERTY, A., AND GOLLUB, J. P., *Self-affine fractal interfaces from immiscible displacement in porous media*. Phys. Rev. Lett. **63** (1989) 1685–1688.

[50] SURDEANU, R., WIJNGAARDEN, R. J., VISSER, E., HUIJBREGTSE, J. M., REC-
TOR, J. H., DAM, B., AND GRIESSEN, R., *Kinetic roughening of penetrating flux
fronts in high-T_c thin film superconductors*. Phys. Rev. Lett. **83** (1999) 2054–2057.

[51] SZABÓ, G., ALAVA, M. J., AND KERTÉSZ, J., *Self-organized criticality in the
Kardar-Parisi-Zhang equation*. Europhys. Lett. **57** (2002) 665–671.

[52] TANG, L.-H. AND LESCHHORN, H., *Pinning by directed percolation*. Phys. Rev. A
45 (1992) R8309–R8312.

[53] VILLAIN, J., *Continuum models of crystal growth from atomic beams with and with-
out desorption*. J. Phys. I France **1** (1991) 19–42.

[54] WOLF, D. E. AND KERTÉSZ, J., *Noise reduction in Eden models: I.* J. Phys. A **20**
(1987) L257–L261.

[55] WOLF, D. E. AND TANG, L. H., *Inhomogeneous growth processes*. Phys. Rev. Lett.
65 (1990) 1591–1594.

[56] ZHANG, J., ZHANG, Y.-C., ALSTRØM, P., AND LEVINSEN, M. T., *Modeling for-
est fire by a paper-burning experiment, a realization of the interface growth mechanism*.
Physica A **189** (1992) 383–389.